Characteristics of Multi-scale Current Sheets in the Solar Wind at 1 au Associated with Magnetic Reconnection and the Case for a Heliospheric Current Sheet Avalanche

Stefan Eriksson[1] , Marc Swisdak[2] , James M. Weygand[3] , Alfred Mallet[4] , David L. Newman[5] , Giovanni Lapenta[6,7] ,
Lynn B. Wilson III[8] , Drew L. Turner[9] , and Bjorn Larsen[10]

[1] Laboratory for Atmospheric and Space Physics, University of Colorado, Boulder, CO, USA; eriksson@lasp.colorado.edu
[2] IREAP, University of Maryland, College Park, MD, USA
[3] Institute of Geophysics and Planetary Physics, University of California, Los Angeles, CA, USA
[4] Space Sciences Laboratory, University of California, Berkeley, CA, USA
[5] Center for Integrated Plasma Studies, University of Colorado, Boulder, CO, USA
[6] Department of Mathematics, Katholieke Universiteit Leuven, University of Leuven, Belgium
[7] Space Science Institute, Boulder, CO, USA
[8] NASA Goddard Space Flight Center, Heliophysics Division, Greenbelt, MD, USA
[9] Johns Hopkins University Applied Physics Laboratory, Laurel, MD, USA
[10] Department of Physics, University of Connecticut, Storrs, CT, USA

Abstract

Wind spacecraft measurements are analyzed to obtain a current sheet (CS) normal width d_{cs} distribution of 3374 confirmed magnetic reconnection exhausts in the ecliptic plane of the solar wind at 1 au. The d_{cs} distribution displays a nearly exponential decay from a peak at $d_{cs} = 25$ d_i to a median at $d_{cs} = 85$ d_i and a 95th percentile at $d_{cs} = 905$ d_i with a maximum exhaust width at $d_{cs} = 8077$ d_i. A magnetic field θ-rotation angle distribution increases linearly from a relatively few high-shear events toward a broad peak at $35° < \theta < 65°$. The azimuthal ϕ angles of the CS normal directions of 430 thick $d_{cs} \geqslant 500$ d_i exhausts are consistent with a dominant Parker-spiral magnetic field and a CS normal along the ortho-Parker direction. The CS normal orientations of 370 kinetic-scale $d_{cs} < 25$ d_i exhausts are isotropic in contrast, and likely associated with Alfvénic solar wind turbulence. We propose that the alignment of exhaust normal directions from narrow $d_{cs} \sim 15–25$ d_i widths to well beyond $d_{cs} \sim 500$ d_i with an ortho-Parker azimuthal direction of a large-scale heliospheric current sheet (HCS) is a consequence of CS bifurcation and turbulence within the HCS exhaust that may trigger reconnection of the adjacent pair of bifurcated CSs. The proposed HCS-avalanche scenario suggests that the underlying large-scale parent HCS closer to the Sun evolves with heliocentric distance to fracture into many, more or less aligned, secondary CSs due to reconnection. A few wide exhaust-associated HCS-like CSs could represent a population of HCSs that failed to reconnect as frequently between the Sun and 1 au as other HCSs.

Unified Astronomy Thesaurus concepts: Solar magnetic reconnection (1504); Solar wind (1534); Heliosphere (711); Interplanetary turbulence (830)

1. Introduction

The Sun constantly releases a supersonic wind of plasma and magnetic field from the solar corona into the heliosphere (Parker 1958). This inner heliosphere solar wind is commonly observed to move outward at a radial 250–500 km s^{-1} speed in the ecliptic plane with a fast >600 km s^{-1} solar wind associated with the open magnetic fields of coronal holes (e.g., Phillips et al. 1995; Cranmer 2009; Lionello et al. 2014). The origin of the slow solar wind is less certain, but it is believed to be associated with coronal streamer belts encircling the Sun (e.g., Borrini et al. 1981; Gosling et al. 1981; Marsch 1999).

Parker (1958) first described how the solar magnetic field of the coronal plasma is carried away from the Sun by the solar wind. The solar rotation of the magnetic foot-points of the field and the radial outflow of coronal plasma increasingly bends the solar magnetic field from a dominant radial component close to the Sun into a spiral magnetic field with a dominant azimuthal component far from the Sun. The solar magnetic field at 1 au $= 1.496 \times 10^8$ km heliocentric distance is commonly

observed along a 45° Parker-spiral angle off a radial direction from the Sun (e.g., Luhmann et al. 1993; Chang et al. 2019). This Parker-spiral *away* direction is equivalent to an azimuthal angle $\phi = 135°$ of the solar magnetic field in a Geocentric Solar Ecliptic (GSE) coordinate system defined as $\phi = \arctan(By/Bx)$ with $\phi = 0°$ along $+X_{GSE}$ and $\phi = 90°$ along $+Y_{GSE}$, and it follows that a *toward* Parker-spiral solar magnetic field is equivalent to $\phi = 315°$.

The heliospheric current sheet (HCS) defines the boundary between the open coronal magnetic field directed away from one high-latitude polar region, and the open coronal magnetic field directed toward the other polar region (e.g., Schulz 1973; Jokipii & Thomas 1981; Crooker et al. 1993; Winterhalter et al. 1994; Lepping et al. 1996; Banaszkiewicz et al. 1998; Smith 2001). The HCS encircles the Sun as a folded surface near the equatorial plane as a result of solar rotation that Alfvén (1977) referred to as a *ballerina skirt*. It is often argued that the HCS constitutes the heliospheric extension of a coronal source surface neutral line between the two polarities of the solar magnetic field, which is also known as a coronal streamer belt (e.g., Crooker et al. 1993; Smith 2001), while solar rotation and dipole tilt may contribute to the folds of the HCS (Smith 2001).

Let us define a normal, $N_{GSE} = [Nx, Ny, Nz]$, to this folded HCS surface at 1 au with an azimuthal angle $\phi = \arctan(Ny/Nx)$

in the ecliptic plane and a polar angle $\theta = \arctan(N_E/Nz)$. Here, N_E is the magnitude of the projection of $\mathbf{N}_{GSE}$ onto the ecliptic plane such that $\theta = 0°$ corresponds to a normal along $+Z_{GSE}$ and $\theta = 90°$ is an HCS normal contained in the ecliptic plane ($Nz = 0$). A dominant Parker-spiral solar magnetic field at 1 au along $\phi = 135°$ therefore corresponds to an HCS normal direction with an azimuthal component aligned with the ortho-Parker direction $\phi = 225°$ or $45°$ (Lepping et al. 1996).

Winterhalter et al. (1994) analyzed the normal widths for 19 well-isolated HCS crossings at 1 au. They first defined an HCS normal width $d_{cs} = \Delta t_{cs} |\mathbf{N} \cdot \mathbf{V}_{sw}|$, where Δt_{cs} is the duration of a continuous rotation of the maximum variance component of the magnetic field (Sonnerup & Cahill 1967) from one side of the HCS to the other side of the HCS. Importantly, they also applied a normal component of the solar wind velocity (V_{sw}) by which the HCS moved over the ISEE 3 spacecraft, where $\mathbf{N}$ is the direction of minimum variance of the high-cadence (6 Hz) magnetic field. This analysis resulted in a median $d_{cs} = 9100$ km normal width of the HCS with a range of 3500–12,000 km. The individual HCS normal widths are, perhaps, surprisingly narrow if we consider that the Wind spacecraft obtained a median $d_i = 97.6$ km ion inertial length at 1 au (Klein & Vech 2019). Here, 1 $d_i = c/\omega_{pi}$ is the ion inertial length, where c is the speed of light and $\omega_{pi} = \sqrt{(N_p e^2/m_p \epsilon_0)}$ is the proton density (N_p) dependent plasma frequency.

Lepping et al. (1996) used Wind spacecraft observations to examine a subset of 212 HCS encounters during an approximate 5 month long interval with the requirement that each HCS had to satisfy a $\geqslant 130°$ rotation of the azimuthal component of the solar magnetic field. This criterion reflected their assumed *definition of an individual HCS crossing* as a *field transition through about 180° in no more than tens of minutes*. They subsequently assumed a 420 km s^{-1} radial solar wind flow to report an average thickness of 64,000 km. This average HCS width is certainly an overestimate of the actual HCS normal widths of the analyzed events, given the radial flow speed assumption and the histogram distributions of the azimuthal and polar angles of the HCS normal direction also reported by Lepping et al. (1996). However, it appears that the normal width of the HCS can be expected in a very broad range at 1 au from ~35–120 d_i (Winterhalter et al. 1994) to ~600–700 d_i widths (Lepping et al. 1996) for a statistical median $d_i \sim 100$ km.

Any given HCS encounter is often associated with many current sheet (CS) crossings occurring over a period that may last up to 1–2 days (e.g., Crooker et al. 1993; Winterhalter et al. 1994; Smith 2001), which is short compared with a 27 day solar rotation period. There is no conclusive interpretation of this swarm of HCS crossings at 1 au on the basis of single spacecraft observations. Early suggestions have included a wave-like signature of the HCS, or multiple helmet streamers associated with multiple parallel CSs, extending out into the heliosphere from the corona (Crooker et al. 1993).

The coherent HCS feature that we ultimately associate with a rotation of an open Parker-spiral solar magnetic field, whether consisting of one or multiple parallel layers of current, is not the only source of CS-associated magnetic field rotations in the 1 au solar wind. At the lower end of a normal width distribution, Vasquez et al. (2007) performed a statistical study of kinetic-scale CSs in 3 Hz cadence magnetic field observations from the ACE spacecraft during a 27 day solar rotation period. This study reported a most probable ~4 d_i normal width for small $3° < \theta < 30°$ magnetic field rotation angles across the CSs, and

a most probable ~8 d_i normal width for magnetic field rotation angles $\theta > 30°$. Analyses of 17,043 kinetic-scale CSs with normal widths on the order of 0.1–10 d_i by Vasko et al. (2022) resulted in a correlation between this θ-rotation angle and a CS normal width (d_{cs}) in the solar wind at 1 au such that $\theta \sim 19°(d_{cs}/d_i)^{0.5}$. Vasquez et al. (2007) first associated the source and clustering tendency of kinetic-scale CSs with Alfvénic turbulence in the ecliptic plane of the solar wind. It is well known that the solar wind is in a state of varying degree of turbulence, as reviewed by Bruno & Carbone (2013), from in situ measurements in the ecliptic plane (e.g., Matthaeus & Goldstein 1982) and out of the ecliptic plane (e.g., Chen et al. 2012). Numerical simulations of MHD turbulence further support the formation of coherent structures such as CSs and magnetic islands (e.g., Matthaeus & Lamkin 1986; Servidio et al. 2009, 2010; Zhdankin et al. 2013; Mallet et al. 2016; Dong et al. 2018).

CSs near the ecliptic plane of the solar wind at 1 au, whether associated with a source in solar wind turbulence or with a source in a coronal streamer belt, may disrupt due to a magnetic reconnection tearing instability (e.g., Priest & Forbes 2000) as first reported by Gosling et al. (2005a). Magnetic reconnection is a fundamental plasma physics process that changes the connectivity of magnetic fields within a highly localized region of a CS and allows plasmas to mix across the boundary. Birn et al. (2001) show how a critical CS thickness on the order of 1–2 d_i can lead to an explosive type of tearing-mode reconnection (Lakhina & Schindler 1983; Drake et al. 1983).

A major characteristic of reconnection is the conversion of magnetic energy into plasma acceleration from the topological X line in two opposite jets along the CS (e.g., Davis et al. 2006; Eriksson et al. 2009). The maximum jet speed in the CS frame of reference is theoretically limited to the Alfvén speed of the ambient plasma. The jets subsequently expand in a normal direction with downstream distance from the X line into two reconnection exhausts. The opening angle of this normal exhaust expansion is limited to the rate of reconnection at the X line. However, Shepherd et al. (2017) caution that the out-of-plane component of the magnetic field may force the exhaust to remain collimated in a normal direction beyond a critical distance from the X line. An important consequence of this collimation process is that a fraction of solar wind exhausts may not necessarily represent an ever-expanding jet population originating from distant reconnection X lines in very extended and thin, kinetic-scale CSs.

The MMS satellites have encountered many X-line electron diffusion regions in the Earth's magnetosphere (e.g., Burch et al. 2016a, 2016b; Eriksson et al. 2016; Webster et al. 2018). There are no reports of such fortunate encounters in the vastness of the solar wind. However, there are plenty of Alfvénic reconnection outflows of varying normal widths in the solar wind as recorded by different spacecraft at 1 au (e.g., Gosling et al. 2005a; Phan et al. 2006, 2009, 2010; Eriksson et al. 2009, 2014, 2015; Pulupa et al. 2014; Enžl et al. 2014; Mistry et al. 2016, 2017), Ulysses observations of 91 exhausts beyond 1 au (Gosling et al. 2006a), Helios observations at 0.3–1 au (Gosling et al. 2006b), and Parker Solar Probe observations much closer to the Sun (e.g., Phan et al. 2020, 2021).

Osman et al. (2014) employed a method of partial variance increment on 3 s cadence magnetic field measurements to identify 521 CSs deemed to be associated with reconnection exhausts as recorded by the Wind spacecraft to suggest that reconnecting CSs are concentrated in periods of intermittent

turbulence in the solar wind. Numerical simulations and in situ observations indeed seem to suggest that turbulence and magnetic reconnection may be two intricately linked processes (Gosling 2007; Retinò et al. 2007; Lapenta 2008; Cho & Lazarian 2009; Servidio et al. 2012; Osman et al. 2014; Loureiro & Boldyrev 2017; Mallet et al. 2017; Dong et al. 2018). Lazarian & Vishniac (1999) proposed that turbulence may enhance the rate of reconnection, and Lazarian et al. (2020) even imply that turbulence may determine the reconnection rate in realistic 3D, large-scale astrophysical systems such as the solar wind.

A major outstanding question, despite all of the reconnection exhaust evidence amassed so far in the ecliptic plane of the solar wind at 1 au, is whether intermittent turbulence of the solar magnetic field drives the process of CS formation and subsequent magnetic reconnection, as first envisioned by Matthaeus & Lamkin (1986) and Osman et al. (2014), and later modeled by Loureiro & Boldyrev (2017) and Mallet et al. (2017), or whether magnetic reconnection X lines and their downstream exhausts lead to the observed intermittent turbulent behavior of solar wind CSs, as implied by Lapenta (2008) and Lapenta & Lazarian (2012). In other words, is it possible that the 1 au solar wind may support two scale-dependent regimes, wherein one scenario dominates the other?

Section 2 of this paper describes the sliding window method that we used to identify reconnection exhausts across solar wind CSs in the Wind spacecraft observations, and we provide a few initial examples of exhausts at relatively small scales. Section 3 presents a set of histogram distributions of exhausts at 1 au. In Section 4, we first discuss the nature of exhaust-associated CSs and the orientation of their normal directions in the solar wind. We also review what is known about reconnection across the HCS, and discuss the large-scale implication of a commonly observed CS bifurcation across reconnection exhaust layers (Gosling & Szabo 2008) for the evolution of the HCS through multi-scale magnetic reconnection. Section 4 provides a summary and conclusions.

2. CS Identification and Reconnection Exhaust Confirmation

In order to address the fundamental question of the intricate link between turbulence and magnetic reconnection, we opt to exploit the long-term availability of Wind spacecraft measurements (Wilson et al. 2021) from 2004 July 1 to 2014 December 31 in the ecliptic plane of the solar wind to collect a statistically significant sample of reconnection exhausts. We employ magnetic field (B) measurements at 3 s and 92 ms resolution in GSE coordinates from the Wind Magnetic Field Investigation instrument (Lepping et al. 1995) and 3 s cadence plasma measurements of density N_p, proton temperature T_p, and velocity V in GSE coordinates from the Three-Dimensional Plasma (3DP) instrument (Lin et al. 1995).

Individual periods of 3 s cadence B, N_p, and V measurements are obtained from the NASA CDAWeb with the plasma observations first interpolated to the same time as B. The B measurements are then surveyed for changes in any of the three GSE components (Bx, By, Bz) individually within each time period of a sliding window of constant duration that we advance forward in time by the length of the window. In these Wind data, we required $|\Delta Bx| \geqslant 1$ nT or $|\Delta By| \geqslant 1$ nT or $|\Delta Bz| \geqslant 1$ nT in a given time window to be classified as a potential CS. The three components of the average magnetic

field B_1 and B_2 adjacent to each time window containing this change in B are obtained as individual three data-point averages. The magnetic field centered at time periods of potential CSs and the corresponding interpolated V are then rotated from GSE to a boundary-normal coordinate system that we define using a cross-product normal $N = B_1 \times B_2 / |B_1 \times B_2|$. The routine finds a maximum variance L_m direction from a minimum variance analysis of B (Sonnerup & Scheible 1998) across the field gradient. Finally, the two orthogonal unit vectors to N are defined as $M = N \times L_m / |N \times L_m|$, which is also referred to as the out-of-plane or guide-magnetic field direction, and $L = M \times N$, which is close to the direction of maximum variance. In the presence of magnetic reconnection across a CS, this L direction corresponds to the component of the magnetic field that reconnects across the CS and the direction of the reconnection exhaust. This boundary-normal LMN system is more robust than using the three eigenvectors of the minimum variance analysis of B (Knetter et al. 2004; Vasquez et al. 2007). A cross-product normal is also preferred when examining a CS for the presence of a reconnection exhaust for two other reasons. First, particle-in-cell (PIC) simulations of magnetic reconnection show that a CS normal component of B can experience relatively large fluctuations across a CS in the presence of exhaust structure, e.g., magnetic islands (Eriksson et al. 2014, 2015). This variability is suppressed by default along a minimum variance normal direction. Second, PIC simulations typically show a very small magnitude B_N component away from the reconnecting CS layer, which is not always the case when using a minimum variance N direction in the solar wind. Finally, we define a CS from the requirements that the gradient of the B_L component of the surveyed lower-cadence magnetic field across an identified time window be monotonic with $|\Delta B_L| \geqslant 1$ nT and that B_L changes sign.

Each CS is subsequently examined for the presence of a reconnection exhaust following the observation signatures first reported by Gosling et al. (2005a) that B_L and V_L need to be correlated on one side, and anticorrelated on the other side of the CS. In other words, we require that the V_L component of the 3 s (interpolated) V peaks, with $|V_{Lpeak}|$ as the local maximum or local minimum, during the B_L rotation. The jet candidate is obtained as $\Delta V_{L1} = |V_{Lpeak} - V_{L1}|$ on the leading edge of the window, and $\Delta V_{L2} = |V_{Lpeak} - V_{L2}|$ on the trailing edge of the window. Here, V_{L1} and V_{L2} are the two values adjacent to the sliding window. Each exhaust candidate is stored separately for each of the chosen time windows for later consideration of whether it may also satisfy the Walén relation $V_{WL} = V_{L0} \pm \Delta V_{AL}$ as expected for a magnetic reconnection exhaust (Paschmann et al. 1986), where ΔV_{AL} is given as

$$\Delta V_{AL} = \sqrt{\rho_0 / \mu_0} \; (B_L / \rho - B_{L0} / \rho_0).$$

Here, $\mu_0 = 4\pi \times 10^{-7}$ Vs/Am is the permeability of free space and the other parameters indicated with a subscript "0" (V_{L0}, B_{L0}, ρ_0) correspond to the given external parameter at the start time of the Walén prediction, whether that is before the CS (leading side) or after the CS (trailing side). The positive and negative signs of ΔV_{AL} are chosen automatically according to the direction of the potential jet ($\Delta V_L > 0$ or $\Delta V_L < 0$).

The reconnection exhaust confirmation is conducted semi-manually for each unique jet candidate as follows. We first obtain the original Wind B and V data in a GSE coordinate system, rotate the 3 s cadence V and the high-cadence 92 ms B

from GSE to the preliminary LMN system as previously stored from the initial CS survey, and manually select new times adjacent to the highly resolved CS using software publicly available from the SPEDAS libraries (Angelopoulos et al. 2019). This allows us to obtain a revised determination of the cross-product normal N vector and to update the pseudo-maximum variance L vector and the M vector accordingly for an optimized LMN system. This optimization step is taken, since the times of the automated sliding window procedure that applies a lower-cadence B may have clipped a local CS when viewed in a higher 92 ms cadence B. We subsequently rotate the 3 s V and the 92 ms B from GSE to the revised LMN system and determine the actual CS duration by selecting a start time and a stop time of the B_L rotation period of the CS on the basis of the high-cadence B_L. Finally, we examine whether the suggested enhancement of the plasma flow across the CS is consistent with a magnetic reconnection exhaust by performing the Walén test $V_{WL} = V_{L0} \pm \Delta V_{AL}$ on the L component of the proton velocity (V_L) based on a tangential momentum balance (e.g., Sonnerup et al. 1981; Paschmann et al. 1986; Eriksson et al. 2009, 2014). This test is performed from each side of all CSs separately, since V_L and B_L need to be in phase across one exhaust boundary and they need to be out of phase across the other exhaust boundary. The Walén test applies the high-cadence B_L magnetic field at 92 ms and a mass density $\rho = N_p m_p$ interpolated to this B_L.

We applied the sliding window on Wind spacecraft measurements using different time-averaged Δt_{avg} cadence data for a total of six sliding window durations: $\Delta t = 12$ s, 18 s, 2 minutes, 4 minutes, 10 minutes, and 20 minutes from 2004 July 1 to 2014 December 31. Here, $\Delta t_{avg} = 3$ s cadence data are used for the small windows, $\Delta t = 12$ and 18 s, time-averaged $\Delta t_{avg} = 1$ minute data are used for the intermediate duration windows $\Delta t = 2$ and 4 minutes, and time-averaged $\Delta t_{avg} = 5$ minute data are used for the long-duration windows $\Delta t = 10$ and 20 minutes. The six sliding window surveys resulted in a total of 3374 confirmed reconnection exhausts following the Walén analysis from an initial pool of 4945 candidate exhaust events. The discarded events were associated with data gaps, data spikes, underresolved CSs in plasma data, or displaying an Alfvénic perturbation of only one sense (correlated or anticorrelated B_L and V_L) across the entire CS. The set of 3374 exhaust-associated CSs that the Wind spacecraft encountered should be considered as the tip of the proverbial iceberg, if we consider that many other discrete time duration windows can be applied to Wind spacecraft measurements for this 10 yr interval. However, the confirmed exhaust-associated CSs represent a statistically significant data set as compared with the 188 exhausts reported by Mistry et al. (2017), 197 exhausts by Phan et al. (2010), 418 exhausts by Enžl et al. (2014), or 521 exhausts reported by Osman et al. (2014), all of which also relied on Wind spacecraft observations due to its long-term presence collecting 3 s cadence plasma observations in the solar wind.

Figure 1 illustrates the measurements of magnetic field (panels (a)–(c)), proton velocity (panels (d)–(f)), plasma number density (g), proton and electron temperatures (h), pressures (i), and plasma β (j) for three examples of confirmed reconnection exhausts in their individual LMN coordinate systems. The electron temperature (T_e) and electron plasma pressure (P_e) are measured by the Solar Wind Experiment (SWE) instrument (Ogilvie et al. 1995; Wilson et al. 2018) at 9 s cadence or longer. The total pressure $P_{tot} = P_B + P_p + P_e$, as displayed in Figure 1(i), is shown at the 3 s cadence of the proton plasma pressure (P_p) with the 92 ms

magnetic field pressure (P_B) and the variable cadences of P_e interpolated to the fixed 3 s cadence of P_p to indicate whether a given exhaust-associated CS is in overall pressure balance. The total plasma $\beta = (P_e + P_p)/P_B$ is analyzed at the SWE instrument cadence.

The three examples of exhaust shown in Figure 1 were identified using three different durations of a sliding window with $\Delta t = 12$ s (left), $\Delta t = 18$ s (middle), and $\Delta t = 2$ minutes (right). The actual durations of these CSs, which are indicated between the two vertical dashed lines, are $\Delta t_{cs} = 10.9$ s, $\Delta t_{cs} = 13.3$ s, and $\Delta t_{cs} = 58.0$ s with normal widths $d_{cs} = 14.5$ d_i, $d_{cs} = 34.5$ d_i, and $d_{cs} = 149.6$ d_i. The normal widths were obtained as $d_{cs} = \Delta t_{cs}|N \cdot V_{sw}|$ or $d_{cs} = \Delta t_{cs} V_{Navg}$, where $V_{Navg} = (V_{N1} + V_{N2})/2$ with V_{N1} and V_{N2} being the average normal component of the solar wind velocity before and after the CSs. In the three cases shown in Figure 1, $V_{Navg} \sim 89$ km s^{-1}, $V_{Navg} \sim 232$ km s^{-1}, and $V_{Navg} \sim 384$ km s^{-1}, respectively (see Figure 1(f)), while the average ion inertial lengths are $d_i = 67$ km, $d_i = 89$ km, and $d_i = 149$ km. The CS start and stop times are listed in Table 1 for the three exhausts as well as the CS normal speeds, normal widths, and the magnetic field rotation angle $\theta = \mathrm{acos}(B_1 \cdot B_2)$ across each CS, where B_1 and B_2 are the time-averaged magnetic fields at the leading and trailing edges of the CSs. Table 1 also includes the N_{GSE} and L_{GSE} unit vectors of the CSs in GSE coordinates. The third M_{GSE} unit vector is obtained as $M_{GSE} = N_{GSE} \times L_{GSE}$.

The jet speeds measured from the two sides of the external V_L flows (see Figure 1(d)) into the exhaust are as low as [ΔV_{L1}, ΔV_{L2}] = [9.6, 13.1] km s^{-1} for the first event (Figure 1, left) and only [ΔV_{L1}, ΔV_{L2}] = [9.1, 6.6] km s^{-1} for the second event (Figure 1, middle). The low jet speeds are due to low magnetic field rotation angles of just $\theta = 34°$ across the first CS and $\theta = 21°$ at the edges of the second CS with an associated smaller reconnecting B_L component of B, and the relatively high solar wind Alfvén Mach numbers of $M_A \sim 7.2$ adjacent the first CS and $7.9 < M_A < 8.1$ adjacent the second CS. These M_A values were obtained from the total magnitude of B (see Figure 1(a)). In contrast, the 58 s duration event (Figure 1, right) supported an unusually fast jet at [ΔV_{L1}, ΔV_{L2}] = [107.5, 116.5] km s^{-1}, which is due to the amount of available ΔV_{AL} on the two sides of the CS as a result of a higher $\theta = 75°$ and an unusually low Alfvén Mach number $2.7 < M_A < 2.9$ in the two regions adjacent this exhaust. The predicted outflow velocities, based on the high-cadence B_L of Figure 1(b) and the interpolated plasma density N_p of Figure 1(g), agree with the observed outflows, as demonstrated from the two $V_{WL} = V_{L0} \pm \Delta V_{AL}$ predictions from the two sides of each CS and shown in Figure 1(d) as the red and blue colored traces, respectively.

3. Statistical Exhaust Histogram Distributions at 1 au

Figure 2 demonstrates several important results on the basis of histogram distributions for a number of parameters associated with the Wind spacecraft observations of 3374 confirmed reconnection exhausts across CSs at 1 au. The number of records in each bin of a particular size is the result of applying the previously stated set of six discrete sliding windows through the Wind measurements. Each histogram generally displays four vertical lines. A red solid line marks the peak of a distribution and a bold dashed line marks the location of the median of a cumulative distribution function (CDF). Two thin dashed lines mark the 5th and 95th percentiles of the CDFs. The four associated parameter values are stated in each panel including the
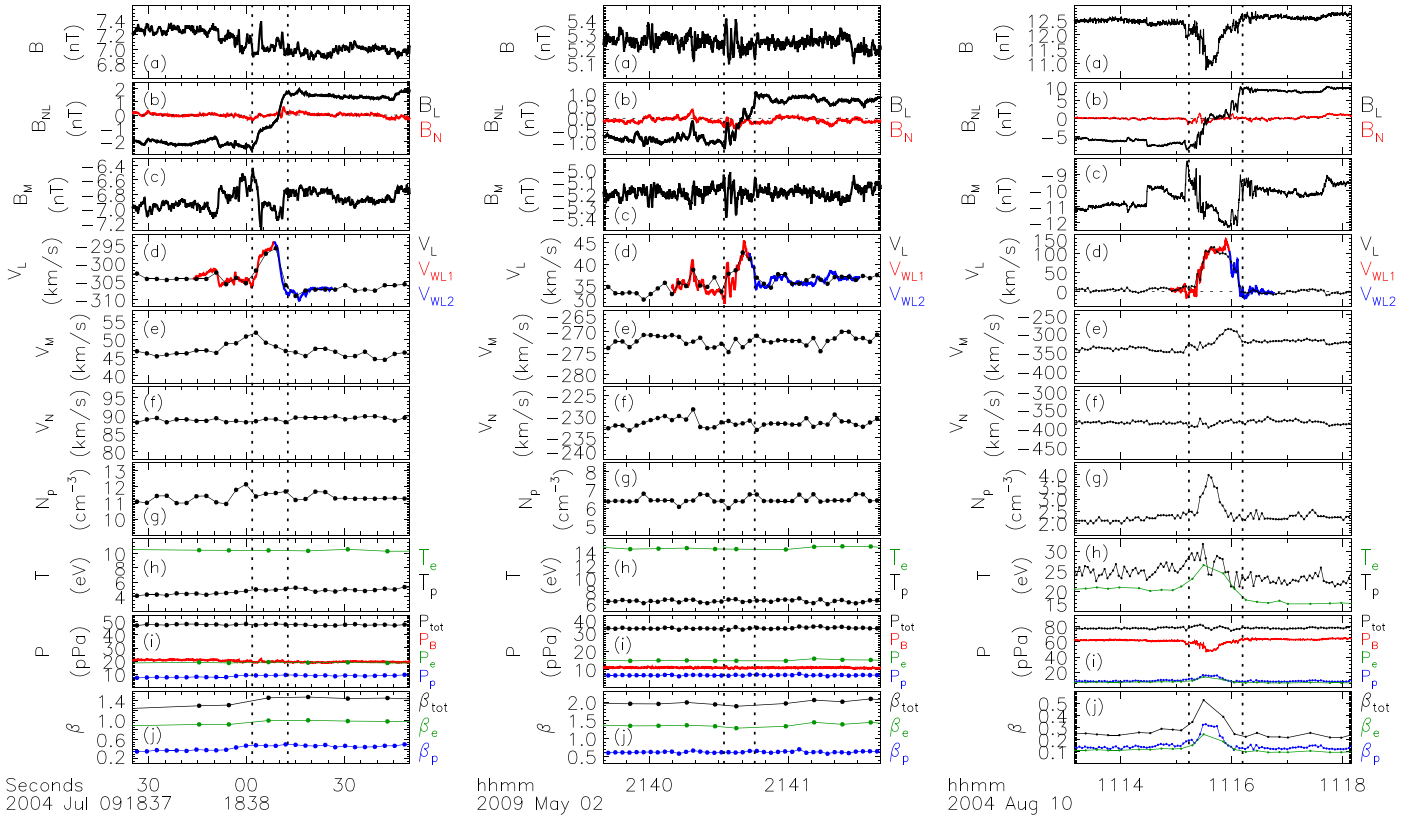
Figure 1. Three examples of Wind reconnection exhausts are shown in their local LMN systems at 18:37:25–18:38:50 UT on 2004 July 9 (left), 21:39:40–21:41:40 UT on 2009 May 2 (middle), and 11:13:10–11:18:10 UT on 2004 August 10 (right). The panels show (a) $|\mathbf{B}|$, (b) B_L (black) and B_N (red), (c) B_M, (d) measured ion velocity V_L and predicted ion velocity V_{WL} from the two-sided Walén relation in red (V_{WL1} leading edge) and in blue (V_{WL2} trailing edge), (e) V_M, (f) V_N, (g) proton density N_p, (h) average temperatures for protons (T_p in black) and electrons (T_e in green), (i) pressures (proton plasma pressure P_p; electron plasma pressure P_e; magnetic field pressure P_B; total pressure $P_{tot} = P_p+P_e+P_B$), and (j) proton $\beta_p = P_p/P_B$ (blue), electron $\beta_e = P_e/P_B$ (green) and total $\beta_{tot} = \beta_p+\beta_e$ (black). The plasma measurements are shown at 3 s resolution (3DP proton data), typically ~ 9 s resolution (SWE electron data), and magnetic field data are shown at 92 ms cadence. A pair of vertical dashed lines mark the start and stop times of the CS and the associated exhaust for each event.

bin size of the distribution. Many histograms are associated with extended tail distributions of fewer counts per bin. As a result, we truncated most histograms at some value beyond the 95th percentile mark to allow for an optimum view of the bulk of the distribution.

Figure 2(a) shows the distribution of actual CS durations with a peak at $\Delta t_{cs} = 10$ s, a median at $\Delta t_{cs} = 40$ s, and a 95th percentile at $\Delta t_{cs} = 340$ s for a 5 s bin size. Figure 2(b) shows the d_{cs} distribution of CS normal widths associated with reconnection exhausts in the ecliptic plane at 1 au with a peak at $d_{cs} = 25 \ d_i$ and a median at $d_{cs} = 85 \ d_i$. The d_{cs} distribution supports an extended tail with the 95th percentile of the cumulative normal width distribution at $d_{cs} = 905 \ d_i$ for a bin size of 5.0 d_i. There are 144 exhausts beyond the displayed 1000 d_i maximum of this d_{cs} distribution with the widest exhaust of the study discovered at $d_{cs} = 8077 \ d_i$. The 144 exhausts are distributed as shown in Table 2. It would seem that CSs in a range $d_{cs} > 9000 \ d_i$ are not very likely to be associated with a reconnection exhaust observation at 1 au from this distribution of exhaust-associated CS normal widths. This result could potentially also reflect a general absence of CSs associated with normal widths >9000 d_i in this sliding window survey for a maximum $\Delta t = 20$ minute window.

The 5th percentile of the d_{cs} distribution at $d_{cs} = 10 \ d_i$ and the apparent drop-off from a peak at $d_{cs} = 25 \ d_i$ inevitably reflects the limitation of the 3 s cadence of the Wind 3DP plasma instrument to resolve more reconnection exhausts in

this kinetic-scale regime of CSs in the solar wind (e.g., Vasquez et al. 2007; Vasko et al. 2022). The fact that Wind could even resolve any exhaust in this kinetic regime is due to fortunate CS orientations relative to the solar wind velocity and a variable plasma-density dependent d_i parameter.

Figure 2(c) displays the distribution of solar wind speeds (V_{sw}) at the leading edge of the events. It shows a broad distribution with 90% of all cases occurring at speeds in the 290–560 km s^{-1} range for a $V_{sw} = 370$ km s^{-1} median, and with the upper 5% of the exhaust distribution occurring at speeds $V_{sw} > 560$ km s^{-1} that we typically associate with ICMEs and fast solar wind streams originating from coronal holes. Figure 2(f) displays the V_{sw} distribution of the 1 hr cadence solar wind speed measurements from the ACE spacecraft for the same overlapping 10 yr interval at a similar upstream L1 location as the Wind measurements of this study of exhausts. This comparative ACE distribution contains 90% of solar wind speeds at 280–610 km s^{-1} with the upper 5th percentile of the CDF found at similarly fast $V_{sw} > 610$ km s^{-1} solar wind speeds. The exhaust-associated V_{sw} distribution at the Wind spacecraft is not that different from this background V_{sw} distribution at ACE for the same time period and a similar L1 location. Both V_{sw} distributions, e.g., display a shoulder near $V_{sw} \sim 600$ km s^{-1}, which is likely due to a population of high-speed streams. In other words, reconnection exhausts should be expected across CSs of any solar wind speed regime.

Figure 2 also displays the distribution of the leading-edge exhaust flows (ΔV_{L1}) in two different ways. First in units of

Table 1
Start (t_1) and Stop (t_2) Date/Times in the Format yyyymmdd/hh:mm:ss.s of Several Exhaust-associated CSs Including the CS Normal Speed, Width (d_{cs}), Magnetic Field Rotation Angle, and the CS Unit Vectors N_{GSE} and L_{GSE} for Each Event

t_1 (UT)	t_2 (UT)	$\lvert V_{Navg}\rvert$ (km s^{-1})	d_{cs} (d_i)	θ (°)	N_{GSE}	L_{GSE}
20040709/18:38:01.7	20040709/18:38:12.6	89	14.5	34	[−0.28134, 0.43754, −0.85405]	[0.94984, 0.00032, −0.31274]
20090502/21:40:32.2	20090502/21:40:45.5	232	34.5	21	[0.59311, −0.31899, −0.73923]	[−0.01668, 0.91310, −0.40740]
20040810/11:15:14.0	20040810/11:16:12.0	384	149.6	75	[0.83240, 0.50608, 0.22579]	[0.00074, −0.40845, 0.91278]
20041010/15:15:09.4	20041010/15:15:19.9	249	26.8	85	[0.64484, 0.59480, 0.48000]	[0.18130, −0.72912, 0.65994]
20070930/11:32:14.2	20070930/11:32:29.8	310	28.8	105	[0.44878, −0.75076, 0.48473]	[0.80807, 0.57255, 0.13863]
20100531/12:25:34.4	20100531/12:25:45.6	558	52.8	77	[−0.94192, −0.26300, −0.20885]	[−0.26925, 0.96307, 0.00156]
20080712/00:29:10.0	20080712/00:29:54.0	393	210.3	67	[−0.82146, −0.46223, −0.33399]	[−0.47967, 0.87680, −0.03368]
20041008/07:05:42.0	20041008/07:07:56.0	279	784.0	132	[−0.86294, −0.29131, −0.41289]	[−0.46755, 0.77023, 0.43375]
20100824/03:07:30.0	20100824/03:17:20.0	359	3996.0	165	[0.80191, 0.08113, 0.59191]	[−0.48372, 0.66964, 0.56355]
20130519/15:56:36.0	20130519/15:57:42.0	335	220.1	63	[0.87468, 0.21288, 0.43544]	[0.03437, 0.86889, −0.49381]
20120924/13:10:34.0	20120924/13:11:42.0	278	220.7	61	[0.80365, 0.39912, 0.44141]	[−0.49770, 0.04414, 0.86622]

kilometers per second with a modest median of $\Delta V_{L1} = 15$ km s^{-1} and a 95th percentile at $\Delta V_{L1} = 50$ km s^{-1} as shown in Figure 2(d), and also as a normalized ratio $\lvert\Delta V_{L1}\rvert/\lvert\Delta V_{WL1}\rvert$ as shown in Figure 2(e). Here, $\lvert\Delta V_{WL1}\rvert = \lvert V_{WL}\text{-}V_{L1}\rvert$ and V_{WL} is the predicted maximum value of the speed of the exhaust from the Walén relation. Most cases display $\lvert\Delta V_{L1}\rvert/\lvert\Delta V_{WL1}\rvert < 1$, which is consistent with previous findings (e.g., Phan et al. 2020), although not yet fully understood. That is, measured exhaust speeds are often somewhat slower than predicted by the Walén relation in the solar wind.

Figure 2(g) displays the distribution of the proton plasma β_{p1} at the leading edge of the exhaust-associated CSs with 90% of the 3374 events found at $0.05 < \beta_{p1} < 2.15$ and a median $\beta_{p1} = 0.55$ for a 0.05 bin size value, in agreement with earlier reports (e.g., Gosling et al. 2007b; Phan et al. 2009). This typically low-β_p regime essentially reflects a background proton β_p distribution of the solar wind in this same 10 yr period as measured by the ACE spacecraft (not shown) with a most probable (peak) value at $\beta_p = 0.35$, a median $\beta_p = 0.40$, and a 95th percentile of the CDF at $\beta_p = 1.25$ for a 0.05 bin size of the 1 hr cadence ACE observations. Figure 2(h) shows θ, the magnetic field rotation angle (a.k.a. the magnetic field shear angle), across these exhaust-associated CSs. The θ distribution is broad with a median at $\theta = 67.5°$, and it appears that the number of events increases linearly from only a few cases near $170° < \theta < 180°$ toward a broad peak at $35° < \theta < 65°$ with an apparent drop-off at low-shear angles with a 5th percentile at $20.0°$. Figure 2(i) displays the magnitude of the L component of the ion velocity difference across the CS, $\Delta V_{LS} = \lvert V_{L2}\text{-}V_{L1}\rvert$, which is normalized to the difference in the L component of the external Alfvén velocity, $\Delta V_{ALext} = \lvert V_{AL2}\text{-}V_{AL1}\rvert$ across the CS. The 95th percentile of this flow-shear distribution at 0.36 suggests that a critical flow shear $\Delta V_{LS}/\Delta V_{ALext} > 0.5$ along a reconnection jet flow direction may inhibit an onset of magnetic reconnection across a CS as predicted by Cassak & Otto (2011). The 0.10 median of this flow-shear distribution is very similar to the 0.12 median reported by Phan et al. (2020) on the basis of 196 Wind exhausts at 1 au.

Swisdak et al. (2003, 2010) employed a numerical simulation to predict that reconnection should be suppressed if the drift speed of the X line along the CS, due to a plasma pressure gradient across the CS, is faster than the exhaust outflow speed. This suppression prediction may be expressed as $\Delta\beta > 2(L/d_i)\tan(\theta/2)$, where $\Delta\beta = \lvert\beta_2\text{-}\beta_1\rvert$ is the change in total plasma $\beta = (P_p + P_e)/P_B$ and θ is the magnetic field rotation angle across the CS. L is a normal

width of the CS near the X line in terms of the ion inertial length. Figure 3(a) displays the distribution of the total β_1 at the leading edge of a subset of 3011 exhaust-associated CSs for which an electron plasma observation is available from the SWE instrument within 35 s of each of the two CS edges. The median time separation is only 7 s between the SWE measurements and the CSs, while the median of the CDF of the relative total pressure differences across the 3011 CSs is only $\lvert P_{tot2}\text{-}P_{tot1}\rvert/P_{tot1} = 2\%$. The exhaust-associated CSs are in pressure balance. The total β_1 distribution shown in Figure 3(a) peaks at $\beta_1 = 1.3$ with a median $\beta_1 = 1.7$ value for a 0.1 bin size with 90% of all cases occurring at $0.4 < \beta_1 < 6.8$. Figure 3(b) displays the $\Delta\beta = \lvert\beta_2\text{-}\beta_1\rvert$ distribution with a median of the CDF at $\Delta\beta = 0.35$, a 95th percentile at $\Delta\beta = 3.90$, and a maximum $\Delta\beta = 67.7$ value. Figure 3(c) shows the corresponding Wind observations of the field rotation angle θ and the change of this total $\Delta\beta$ across the 3011 exhaust-associated CSs. There are 2600 events in the regime to the left of a thick, solid line for $L \leqslant 1$ d_i and $\Delta\beta < 2(L/d_i)\tan(\theta/2)$ where reconnection should be allowed as also confirmed from the Walén prediction analyses. In using the observed $\Delta\beta$ and θ shear angle of the 2600 exhausts, we find that most of the reconnection exhausts satisfy the $\Delta\beta < 2(L/d_i)\tan(\theta/2)$ condition even with $L \sim 0.22$ d_i as the median of the CS thickness near the X line. This result is in general agreement with earlier reports (Phan et al. 2010; Gosling & Phan 2013). However, there is a noticeable spread in the distribution with 342 events present for $1 < L \leqslant 3$ d_i between the thick, solid line and a middle, thin solid line at $L = 3$ d_i. An additional 41 events are present at $3 < L \leqslant 6$ d_i between the pair of thin lines and there are 28 confirmed exhausts to the right of the thin, solid line for $L > 6$ d_i. The 28 exhausts of this unusual $L > 6$ d_i regime were associated with $8.8 < \Delta\beta < 67.7$ and field shear angles in a range $26° < \theta < 138°$. The large $\Delta\beta$ values correspond to a highly asymmetric total plasma β with an exceptionally high $10.3 < \beta < 79.1$ on the high-β side of the exhaust as compared with the entire β_1 distribution shown in Figure 3(a).

Three reconnection exhausts discovered in this exceptional $\Delta\beta$ regime are displayed in Figure 4 (see Table 1 for CS orientations and θ angles). The narrow $d_{cs} = 26.8$ d_i exhaust of 2004 October 10 (Figure 4, left) even displays a clear bipolar B_M magnetic field across the CS consistent with a Hall magnetic field signature despite a large $\beta_2 = 22.8$ at the trailing edge of the CS and $\beta_1 = 1.4$ at the leading edge. The initial positive-then-negative variation of the B_M component across the $d_{cs} = 52.8$ d_i exhaust on 2010 May 31 (Figure 4, right) is also in agreement with a Hall magnetic field. This beautiful
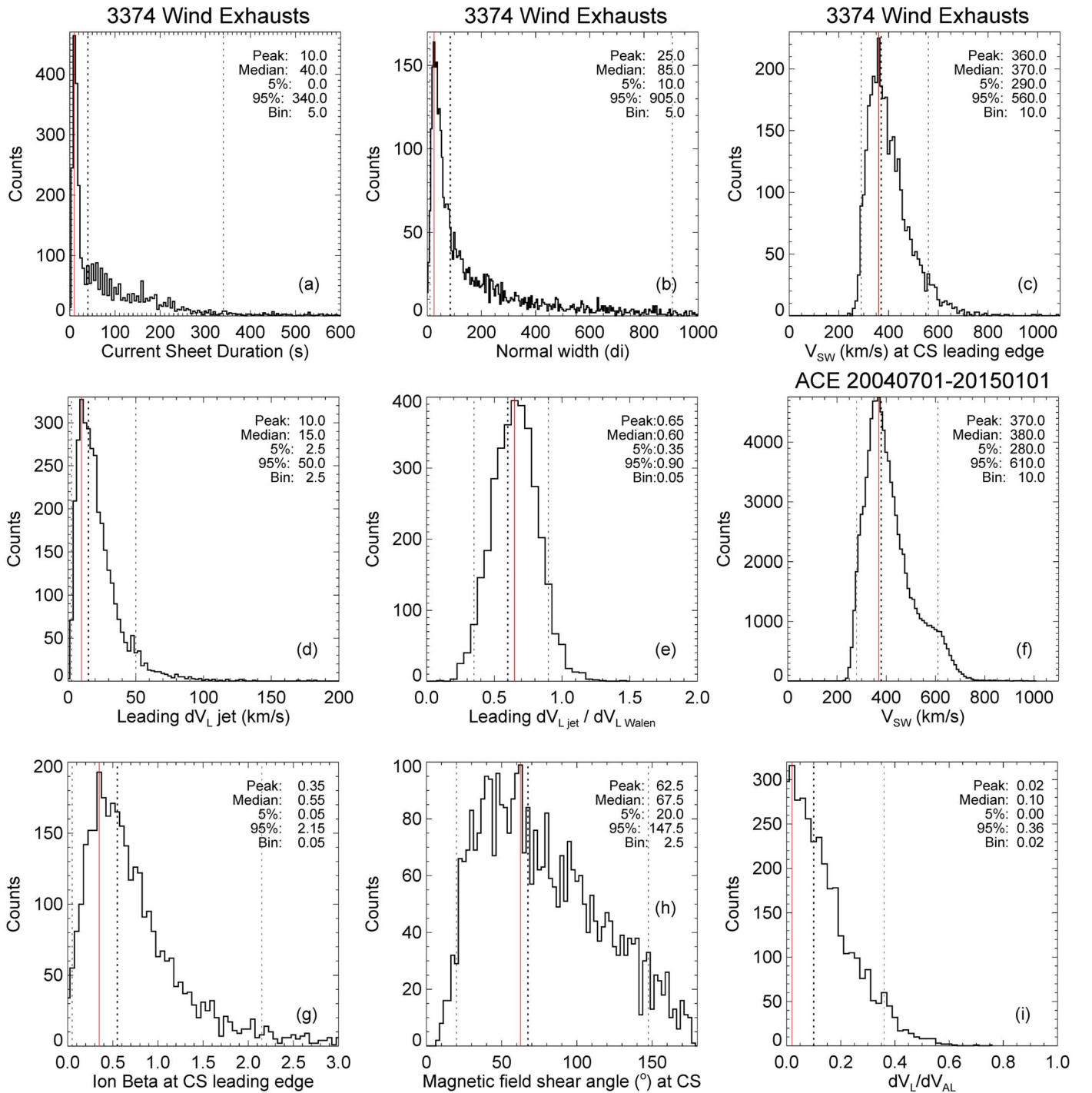
Figure 2. Histograms associated with 3374 solar wind exhausts as observed by the Wind spacecraft from 2004 July 1 to 2014 December 31: (a) CS duration (s), (b) CS normal width (d_i), (c) solar wind speed (km s^{-1}) at the CS leading edge, (d) exhaust speed (km s^{-1}) in the solar wind frame across the CS leading edge, (e) jet speed normalized by the predicted Walén speed, (f) reference solar wind speed distribution as obtained by the ACE spacecraft using all 1 hr data for the same period that overlaps with the Wind study, (g) proton β_{p1} at the CS leading edge, (h) magnetic field shear angle θ (°) across each CS, (i) external flow shear $\Delta V_{LS} = |V_{L2} - V_{L1}|$ normalized by the Alfvén velocity difference $\Delta V_{AL} = |V_{AL2} - V_{AL1}|$ across the CS. Peaks (solid red line) and medians (thick dashed line) are stated as well as the 5th and 95th percentiles of the CDFs (thin dashed lines). Bin sizes are given in their respective units.

exhaust was observed in a presence of $\beta_1 = 1.9$ and $\beta_2 = 17.2$ at the edges of the CS. However, whereas all magnetic field components are highly structured across the $d_{cs} = 28.8$ d_i exhaust on 2007 September 30 (Figure 4, middle), there is a clear presence of a measured V_L reconnection exhaust despite a large $\beta_1 = 24.2$ and $\beta_2 = 1.5$. The total β asymmetries of the three exhausts are primarily reflected as gradients in the proton

plasma pressure and the magnetic field pressure. The electron pressure is less variable as a result of a relatively stable electron temperature across the three CSs as compared with the proton temperature. The three exhausts shown in Figure 4 were also associated with a highly asymmetric B_L rotation with the high β side displaying a weak B_L value and the low β side displaying a significantly stronger B_L component. This was typical of the

Table 2
Distribution of 144 Exhausts with Normal Widths $d_{cs} > 1000 \, d_i$

x1000 d_i	$1 < d_{cs} \leqslant 2$	$2 < d_{cs} \leqslant 3$	$3 < d_{cs} \leqslant 4$	$4 < d_{cs} \leqslant 5$	$5 < d_{cs} \leqslant 6$	$6 < d_{cs} \leqslant 7$	$7 < d_{cs} \leqslant 8$	$8 < d_{cs} \leqslant 9$
Counts	105	21	12	3	1	1	0	1

reconnecting component of the magnetic field in all 28 cases of an exceptionally large $\Delta\beta$ as may be expected from a total pressure balance (e.g., Vasko et al. 2021). Two of the events displayed in Figure 4 were associated with a high $V > 600$ km s^{-1} solar wind speed. However, there are only four cases of this high $\Delta\beta$ regime in a high-speed solar wind $V \geqslant 575$ km s^{-1}, while the median of the other 24 cases displayed a more typical $V_1 = 344.5$ km s^{-1} solar wind speed at the leading edge of the CSs. The high $\Delta\beta$ cases were associated with a wide range of CS normal widths, $19 < d_{cs} < 836 \, d_i$, with a median value of $d_{cs} \sim 126 \, d_i$. In knowing that reconnection was not suppressed across the 28 CSs from the local Wind exhaust observations, we may use the observed values of $\Delta\beta = |\beta_2\text{-}\beta_1|$ and field rotation angle θ of Figure 3(c) for $L > 6 \, d_i$ to estimate the presumed CS normal widths near the X lines. The Wind observations suggest that the X line regions may have been associated with a CS thickness on the order $6.1 < L < 27.2 \, d_i$ with a median $L = 8.8 \, d_i$ normal width for the 28 exhausts that displayed a high β asymmetry.

4. Discussion

A primary motivation of this work is to better understand the intricate relationship between magnetic reconnection and turbulence in the solar wind. The first result that we need to address is the possible origin of the rapidly decaying d_{cs} distribution of exhaust-associated CS normal widths at 1 au (see Figure 2(b)), and by extension the nature of the CSs that support this reconnection activity in the solar wind. It is most definitely true that Wind spacecraft observations contain many more reconnection exhausts that could be identified using several other discrete time window durations than the set of six separate windows applied in this study. However, Figure 2(b) does not indicate any significant breaks of a mostly continuous CS normal width distribution of 3374 exhaust-associated CSs, suggesting that additional exhausts will further build upon the obtained distributions and corroborate that the equatorial plane of the solar wind contains a rapidly decaying distribution of exhaust-associated CS normal widths at 1 au. The prevalence of kinetic-scale CSs in the solar wind for normal widths below the $d_{cs} = 25 \, d_i$ peak of the present Wind exhaust width distribution (Vasquez et al. 2007; Osman et al. 2014; Vasko et al. 2022) certainly means that a true exhaust width distribution, which is only accessible to still higher plasma cadence measurements, will likely peak at a higher number of events and well below $d_{cs} = 25 \, d_i$.

4.1. Exhaust-associated CS Normal Orientations

Let us first examine the orientation of the CS normal directions $N_{GSE} = [Nx, Ny, Nz]$ on the unit sphere for all the 3374 reconnection exhausts. In other words, let us find the two angles θ and ϕ in a spherical coordinate system for each N_{GSE} unit vector, where $\theta = \arctan(N_E/Nz)$ is the polar angle, $\phi = \arctan(Ny/Nx)$ is the azimuthal angle, and N_E is the magnitude of the projection of N_{GSE} onto the ecliptic plane as we also introduced in Section 1. We recall here that the current

density vector itself is directed primarily along M_{GSE} and that the reconnecting component of the magnetic field is aligned with L_{GSE} such that $N_{GSE} \times L_{GSE} = M_{GSE}$.

Figure 5 displays the resulting distribution of spherical angles θ and ϕ for all 3374 CSs associated with a confirmed reconnection exhaust, where we have color-coded a total of five subsets of the full d_{cs} distribution. There are 370 exhausts in a proton kinetic range $d_{cs} < 25 \, d_i$ (blue), 710 exhausts in a super-kinetic range $25 \leqslant d_{cs} < 50 \, d_i$ (light blue), 666 exhausts populated a sub-HCS scale range $50 \leqslant d_{cs} < 100 \, d_i$ (green) with as many as 1198 exhausts in an HCS-like range $100 \leqslant d_{cs} < 500 \, d_i$ (yellow). Finally, there are 430 exhausts that we opt to define as a super-HCS range with normal widths $d_{cs} \geqslant 500 \, d_i$ (red). It appears that these very wide events are particularly concentrated in ϕ space toward $\phi \sim 30°$ and $\phi \sim 210°$ as compared with narrower events. There is also a noticeable absence of cases near $\phi = 90°$ and $\phi = 270°$ as well as $\theta = 0°$ and $\theta = 180°$. Normal directions associated with these spherical angles correspond to orientations of any CS, whereby a spacecraft in the solar wind would spend a significant time traveling along the plane of the CS before making the transition across the CS. That is, the solar wind velocity would in general be nearly aligned with either M_{GSE} or L_{GSE} with a very small normal V_N component of the solar wind velocity adjacent to any such CS. The absence of events near these angles are, at least partially, explained then by a maximum 20 minute window duration in the present survey. The longest exhaust-associated CS duration of this survey is $\Delta t_{cs} = 21.7$ minutes that the Wind spacecraft recorded between 20:49:10.0 UT on 2007 April 5 and 21:10:50.0 UT on 2007 April 5. This event (not shown) was associated with an average $V_N = 230$ km s^{-1} normal component of the solar wind velocity along $N_{GSE} = [0.53616, -0.33341, -0.77548]$ that resulted in a $d_{cs} = 1711 \, d_i$ exhaust normal width.

Figure 6 displays the actual histograms of the azimuthal ϕ angle (panel (a)) and the polar θ angle (panel (b)) of the exhaust-associated CSs shown in Figure 5, using the same color-coded subsets of the CS normal widths as shown in Figure 5. The 430 cases of super-HCS exhausts at $d_{cs} \geqslant 500 \, d_i$ (red) clearly display a preference for a range of azimuthal angles centered about $5° < \phi < 35°$ and $185° < \phi < 215°$, and with a broad range of polar angles centered near $60° < \theta < 120°$. The azimuthal ϕ angles of the very thick CSs are in general agreement with the typical Parker-spiral magnetic field direction at 1 au and a CS normal along the ortho-Parker direction at $\phi \sim 225°$ or $\phi \sim 45°$ (e.g., Lepping et al. 1996). The broad range of polar θ angles centered about $90°$ ($Nz \sim 0$) is consistent with a highly folded or wavy HCS at 1 au (Smith 2001). We interpret these wide CSs as members of the HCS population at 1 au. A pitch-angle distribution of suprathermal strahl electrons as measured by Wind at, e.g., 270 eV (Gosling et al. 2007a) would need to be analyzed to corroborate how close the very thick, exhaust-associated CSs are to a *true* sector boundary, where strahl electrons change between a parallel and antiparallel direction, which is beyond the scope of the present study.

The angular distributions for normal widths in the HCS-like range at $100 \leqslant d_{cs} < 500 \, d_i$ (yellow) are centered about a very
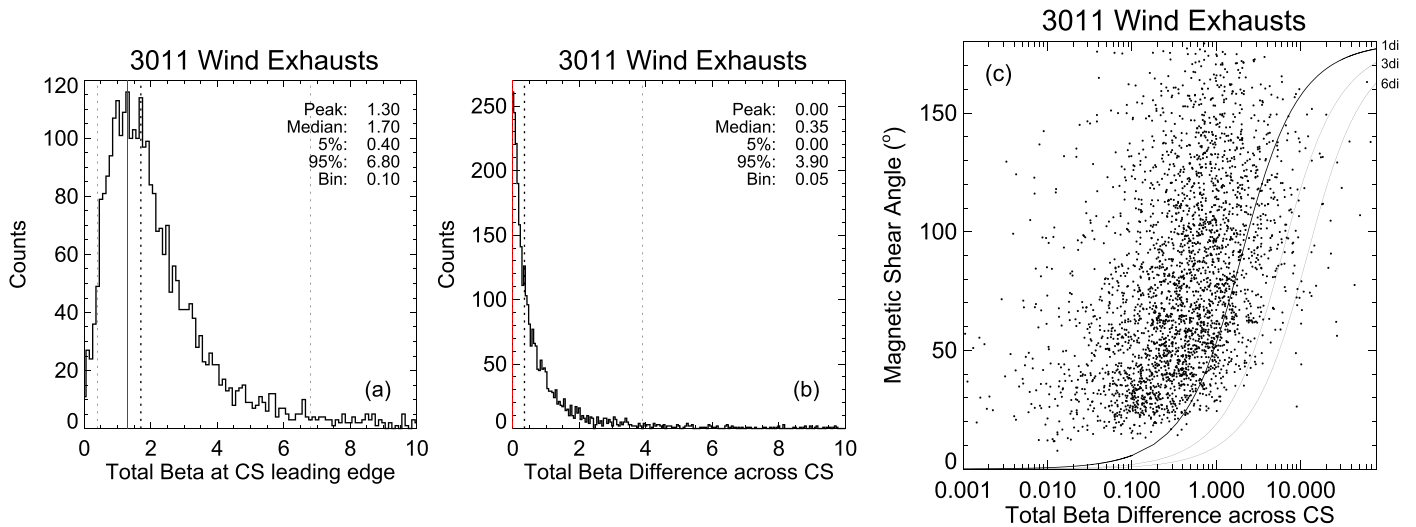
Figure 3. (a) Histogram distribution of total β_1 at the CS leading edge for a subset of 3011 reconnection exhaust-associated CSs for which SWE information is available; (b) histogram distribution of the corresponding change in total $\Delta\beta = |\beta_2\text{-}\beta_1|$ across 3011 CSs; (c) distribution of magnetic field rotation angle θ (degrees) vs. total $\Delta\beta = |\beta_2\text{-}\beta_1|$ difference across all 3011 exhaust-confirmed CSs. The three curves display the function $\Delta\beta = 2(L/d_i)\tan(\theta/2)$ for $L = 1$ d_i (thick solid line), $L = 3$ d_i (middle, thin solid line), and $L = 6$ d_i (right, thin solid line).

similar range of both ϕ and θ angles as the super-HCS population. The broader histogram distributions may be associated with larger statistics of 1198 exhausts for these normal widths. The CS population of 666 exhausts with normal widths in a sub-HCS range $50 \leqslant d_{cs} < 100$ d_i (green) clearly resembles the angle distributions of the two thicker HCS-like distributions. The fact that both angle histograms of cases in this 50–100 d_i range fall between the two HCS-like histograms of 1198 and 430 wider exhausts likely reflects the intermediate counting statistics. That is, the CS normal orientation of these thinner 50–100 d_i CSs associated with reconnection exhausts are also organized by the average solar magnetic field direction at 1 au.

However, the ϕ distribution and the θ distribution of the 370 CS exhaust events in a proton kinetic range ($d_{cs} < 25$ d_i) are essentially isotropic in comparison with the organized CS normal directions for normal widths $d_{cs} \geqslant 50$ d_i. There is nearly no preference for any particular CS normal direction in either azimuthal angles or polar angles with only a few exceptional events at $40° < \phi < 50°$ and $220° < \phi < 230°$. This proton kinetic-range population also tends to be overrepresented in the aforementioned void regions near $\phi = 90°$ and $\phi = 270°$, and they tend to be underrepresented around $\theta \sim 90°$ as compared with the wider $d_{cs} \geqslant 50$ d_i events. We interpret these typically isotropic CS normal directions of thin CSs below 25 d_i as reconnection exhausts associated with true solar wind turbulence in the ecliptic plane at 1 au without a preferred CS normal direction.

Finally, we find that the 710 CS events in a super-kinetic range $25 \leqslant d_{cs} < 50$ d_i (light blue) align their N_{GSE} normal directions near $10° < \phi < 40°$ and $180° < \phi < 230°$ in the ecliptic plane, while showing a broad polar angle range $55° < \theta < 140°$ centered about $\theta \sim 90°$. That is, it appears that these 25–50 d_i wide CSs are associated more with reconnection of the HCS-aligned populations for $d_{cs} \geqslant 50$ d_i than they are with an isotropic, turbulent CS population for $d_{cs} < 25$ d_i. This result is consistent with the narrow ~ 35–120 d_i normal width dimensions of the 19 HCS events reported by Winterhalter et al. (1994).

It may be argued that the exceptional events of the kinetic-scale $d_{cs} < 25$ d_i CSs near $\phi \sim 45°$ and $\phi \sim 225°$ could potentially be members of the same HCS-aligned group of CSs rather than a purely turbulent CS population, although the normal dimension of these exhaust-associated CSs is so narrow compared with the typical expectation of a high-shear and very wide HCS (Lepping et al. 1996). Figure 7 appears to support this suggestion, where a subset of 1746 CSs with normal widths $d_{cs} < 100$ d_i is examined in five groups of nearly equal number of exhausts. Despite a relatively small number of 109 exhausts in the kinetic range $d_{cs} < 15$ d_i (blue) and 261 exhausts in a somewhat wider group at $15 \leqslant d_{cs} < 25$ d_i (light blue), it seems that the exceptional events in the ortho-Parker direction at $\phi \sim 45°$ and $\phi \sim 225°$ of kinetic-scale CSs at $d_{cs} < 25$ d_i (see, e.g., Figure 6(a)) are potential HCS-like members of an exceptionally narrow $15 \leqslant d_{cs} < 25$ d_i population.

4.2. Comparing Reconnection Exhausts across Very Wide CSs at 1 au and Near the Sun

Before we go on to address a potential interpretation of the very smallest spatial scales of the d_{cs} distribution that the Wind spacecraft can resolve at 1 au, we will first review what is known about reconnection across the very wide end of the CS distribution in the solar wind. Understanding these very large-scale CSs is going to be key in also understanding and appreciating the very small-scale end of the d_{cs} distribution. Gosling et al. (2005b, 2006c) reported the very first observations of reconnection exhausts across two confirmed HCS layers at 1 au by the ACE spacecraft. One exhaust was encountered anti-sunward of an X line on 1998 September 17. Gosling et al. (2005b) suggested that the $\theta \sim 141°$ magnetic field rotation of this HCS crossing occurred between $\sim 03:17:33$ and $\sim 03:20:29$ UT from 16 s cadence ACE magnetic field data (Smith et al. 1998) and they proposed a roughly $\sim 53,000$ km thick HCS exhaust. The other HCS-associated exhaust was encountered by ACE on the sunward side of an X line on 1998 December 25 . However, since Gosling et al. (2006c) neither stated the exact time interval of this $\theta \sim 127°$ field rotation, nor the estimated normal width of this HCS exhaust, we first revisit the 1 s cadence ACE magnetic field observations in GSE coordinates to obtain the orientation of the two HCSs on the basis of the same hybrid-LMN system that we employed in this
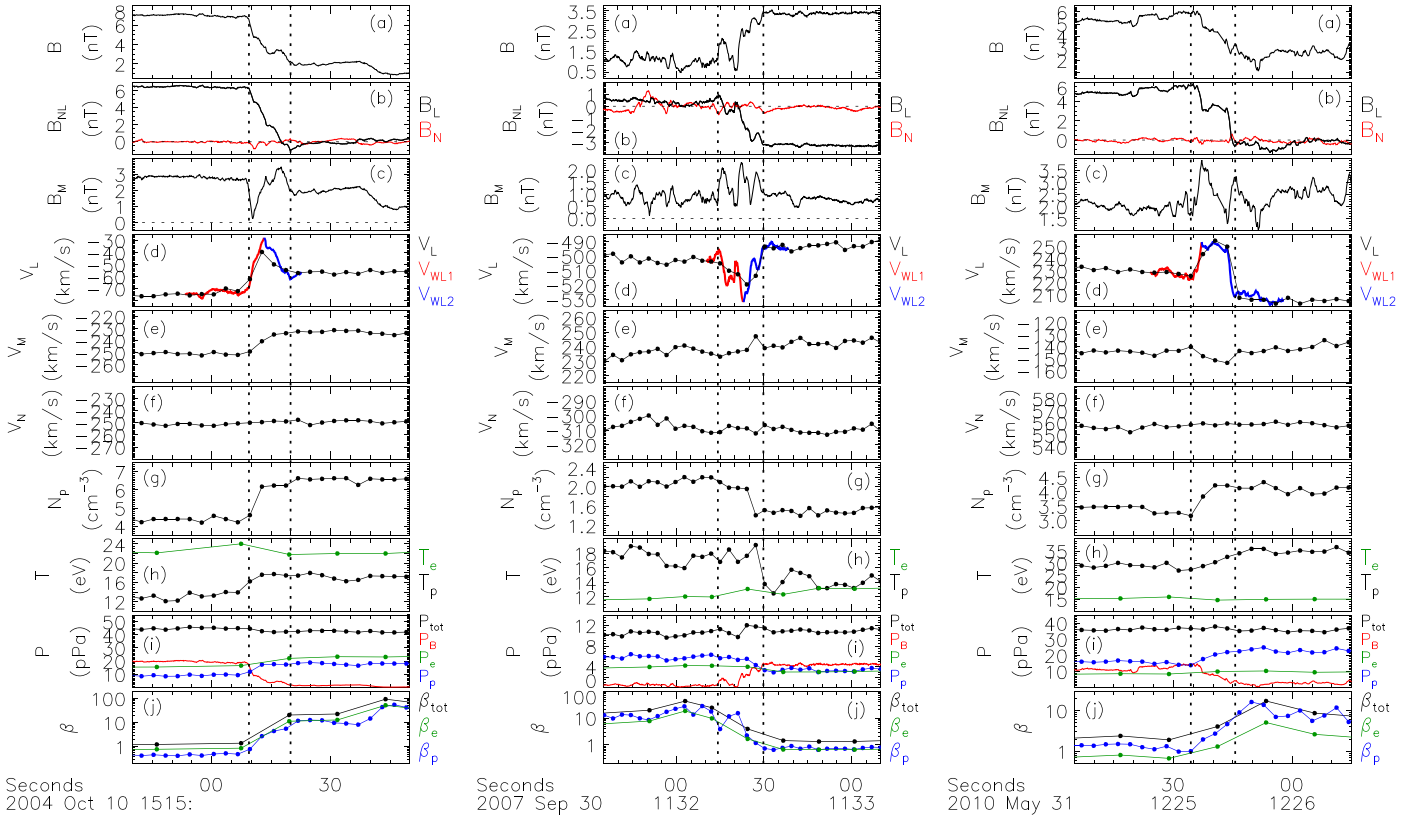
Figure 4. Three examples of Wind reconnection exhausts associated with a significant total β asymmetry in the solar wind are shown in their local LMN systems at 15:14:40–15:15:50 UT on 2004 October 10 (left), 11:31:35–11:33:10 UT on 2007 September 30 (middle), and 12:25:05–12:26:15 UT on 2010 May 31 (right). The format is identical to that of Figure 1.

Wind exhaust survey. The 64 s cadence plasma data from the ACE Solar Wind Electron Proton Alpha Monitor (SWEPAM) instrument (McComas et al. 1998) are available to find a background solar wind velocity in GSE coordinates in both cases. A plasma density is readily available from the SWEPAM instrument on 1998 December 25 with an average $N_p \sim 15.4$ cm^{-3} on the two external sides of the HCS and a corresponding average $d_i = 58.0$ km. The two 12 minute cadence ACE Solar Wind Ion Composition Spectrometer (SWICS; Gloeckler et al. 1998) proton density data points on either side of the HCS event on 1998 September 17 are used to find an average $N_p \sim 8.2$ cm^{-3} and a corresponding $d_i = 79.4$ km.

Table 3 shows the slightly revised HCS times from a rotation of the 1 s cadence B_L component of the magnetic field as well as the N_{GSE} and L_{GSE} directions of the two exhaust-associated HCS events. A somewhat lower 41,204 km or 519 d_i normal width is suggested for the HCS on 1998 September 17, while we obtain a 60,644 km or 1046 d_i normal width for the HCS on 1998 December 25. The N_{GSE} orientations of the two HCS confirmed exhausts correspond to azimuthal angles $\phi \sim 10°$ and $\phi \sim 38°$ with polar angles $\theta \sim 92°$ and $\theta \sim 106°$. That is, the two reported ACE events at 1 au are rather typical cases of the exhaust normal width category of 430 events in the present Wind data survey that we have referred to as super-HCS exhausts with normal widths $500\ d_i \leqslant d_{cs} \leqslant 8077\ d_i$ (see, e.g., Figure 2(b) and Table 2) and a preferred range of azimuthal angles near $5° < \phi < 35°$ and a broad range of polar angles near $60° < \theta < 120°$ (see Figures 5 and 6).

Figure 8 presents three examples of this category of super-HCS ($d_{cs} \geqslant 500\ d_i$) exhausts that we either identified directly from this survey of running windows through Wind spacecraft measurements, or else discovered adjacent to an exhaust-associated CS of the survey. It took the Wind spacecraft $\Delta t_{cs} = 134$ s or 2.2 minutes at an average $V_{Navg} \sim 279$ km s^{-1} normal speed to traverse the first, $d_{cs} = 784\ d_i$ wide exhaust (1 $d_i \sim 48$ km) on 2004 October 8, as indicated in Figure 8 (left) between the two vertical, dashed lines. The predicted jet speed (V_{WL1} and V_{WL2}) was on average ~ 10 km s^{-1} faster than the measured $[\Delta V_{L1}, \Delta V_{L2}] = [27.9, 22.1]$ km s^{-1} jet flow across the complete $\theta = 132°$ magnetic field rotation of this CS as shown in Figure 8(d) (left). Figure 8 (middle) highlights a second, $d_{cs} = 3996\ d_i$ wide V_L exhaust ($V_{Navg} \sim 359$ km s^{-1} and $\Delta t_{cs} = 590$ s or 9.8 minutes) between the two vertical dashed lines on 2010 August 24. Wind measured jet speeds $[\Delta V_{L1}, \Delta V_{L2}] = [-81.6, -80.4]$ km s^{-1} (see Figure 8(d), middle) in good agreement with the predicted outflow velocities, V_{WL1} and V_{WL2}, across the two sides of this very wide and high-shear ($\theta = 165°$) CS from the high-cadence B_L and the interpolated plasma density N_p. The N_{GSE} and L_{GSE} vectors of these CSs of the main survey are listed in Table 1 including the CS start and stop times, normal speeds, d_{cs} widths, and θ angles.

Figure 8 (right) illustrates a third super-HCS example on 2008 July 12 that we discovered immediately adjacent to a relatively low-shear ($\theta = 67°$) and short-duration ($\Delta t_{cs} = 44$ s) exhaust-associated CS of the main survey. That short-duration, $d_{cs} = 210\ d_i$ wide CS, which is also listed in Table 1, is marked in Figure 8 (right) between the first pair of two vertical dashed lines. The complete $\theta = 132°$ magnetic field rotation of the super-HCS event, which is shown for $N_{GSE} = [-0.85149, -0.43257, -0.29641]$, $L_{GSE} = [0.03613, -0.61230, 0.78980]$ and $M_{GSE} = [-0.52313, 0.66179, 0.53699]$, is indicated
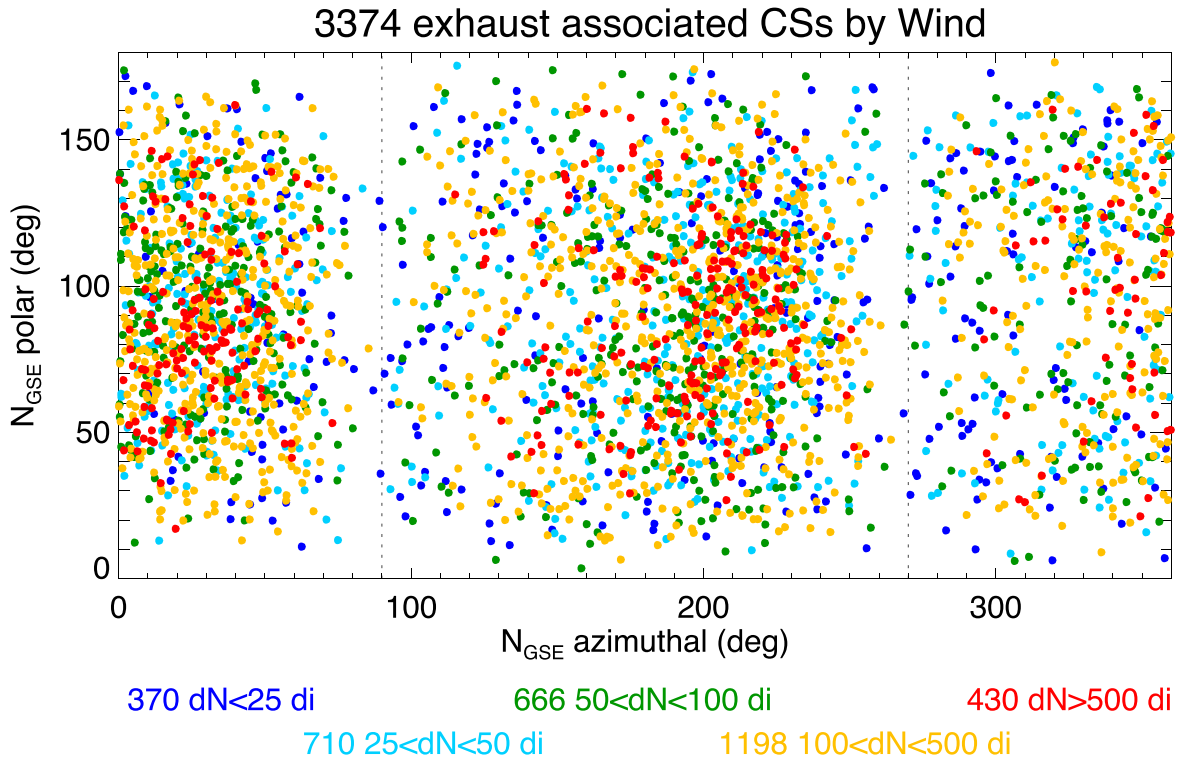
Figure 5. Distribution of spherical polar (θ) and azimuthal (ϕ) angles of the CS normal directions N_{GSE} of 3374 reconnection exhausts. There are five subsets organized by CS normal width d_{cs} for the indicated colors with 370 exhausts in a proton kinetic range $d_{cs} < 25$ d_i (blue), 710 exhausts in a super-kinetic range $25 \leqslant d_{cs} < 50$ d_i (light blue), 666 exhausts in a sub-HCS range $50 \leqslant d_{cs} < 100$ d_i (green), 1198 exhausts in an HCS-like range $100 \leqslant d_{cs} < 500$ d_i (yellow), and 430 exhausts in a super-HCS range $d_{cs} \geqslant 500$ d_i (red).

between the first dashed line at 00:29:10 UT, where $B_L \sim 14$ nT, and a final, green solid line at 01:07:50 UT, where $B_L \sim -13$ nT. This $\Delta t_{cs} = 2320$ s or 38.7 minute duration CS translates to a normal width $d_{cs} \sim 12,233$ d_i (1 $d_i = 78.3$ km) for an average $V_{Navg} \sim 413$ km s^{-1}. The N_{GSE} direction corresponds to an azimuthal $\phi \sim 207°$ angle and a polar $\theta \sim 107°$ angle in agreement with the typical ortho-Parker distributions of super-HCSs recorded by the Wind spacecraft (see Figures 5 and 6). Figure 8(d) illustrating this CS shows a negative $\Delta V_L \sim -60$ km s^{-1} change in the proton velocity as B_L rotates from ~ 14 to ~ 5 nT across the first edge. The proton flow remains at a significant $V_L \sim -50$ km s^{-1} speed across most of the CS until the initial green solid line at 01:00:00 UT, when it displays a positive $\Delta V_L \sim 85$ km s^{-1} change in time, coincident with a B_L rotation of this thick CS from ~ 3 to -4 nT. The negative $\Delta V_L \sim -50$ km s^{-1} flow deflection is typically consistent with a reconnection exhaust across a major section of the complete CS as suggested by a long-duration Walén prediction (see, e.g., first V_{WL1} in red and V_{WL2} in green in panel (d)). The primary exceptions to this overall agreement are two regions of elevated plasma density at $\sim 00:40:00$ and $\sim 00:55:00$ UT deep within the super-HCS when Wind also recorded sizeable B_L fluctuations indicative of internal exhaust structure.

The first $d_{cs} = 784$ d_i wide super-HCS exhaust on 2004 October 8 displays a spectacular CS bifurcation, which is commonly observed (Gosling & Szabo 2008) across many exhaust-associated CSs in the solar wind, with two very sharp (narrow) CSs across each edge of the main exhaust region. A close examination of the B_L component (Figure 8(b), left) appears to show another smaller-scale bifurcation of the first CS. This is highlighted between a pair of solid green vertical

lines at 07:05:46.1 and 07:05:49.8 UT as Wind entered into the exhaust on 2004 October 8. A local $V_{Navg} \sim 279$ km s^{-1} and an average $d_i = 46$ km across this first, $\Delta t_{cs} = 3.7$ s long B_L rotation with a $\theta \sim 75°$ magnetic field shear angle into the main exhaust region corresponds to a narrow $d_{cs} = 22.4$ d_i CS. This normal width represents only 3% of the entire $d_{cs} = 784$ d_i normal width of the primary B_L rotation. A local $N_{GSE} = [-0.83887, -0.21703, -0.49920]$ normal of this first CS is only 6.7° off the main super-HCS normal direction, while the local $L_{GSE} = [-0.53740, 0.47612, 0.69606]$ is 23.1° from the primary exhaust L_{GSE} direction (see Table 1 for N_{GSE} and L_{GSE} of the primary CS). The local $M_{GSE} = [0.08662, 0.85218, -0.51604]$ vector is 24.0° off the M_{GSE} direction of the primary CS. Figure 9 (left) shows a 22 s interval from 07:05:37–07:05:59 UT on 2004 October 8 around this first CS with the components of B_{GSE} and V_{GSE} displayed in the primary LMN coordinate system for sake of clarity. The B_L rotation is clearly bifurcated across this narrow CS with two, discrete steps of B_L. Figure 9(d) (left) compares the Walén prediction of the large-scale V_L exhaust, shown here as the red and blue colored curves as in Figure 8(d) (left), with a localized Walén prediction of the measured V_L component of the solar wind velocity. The local V_L prediction is shown as a slightly thinner green curve. The green Walén prediction follows the red Walén prediction perfectly across a first B_L step, until the second B_L step of this small-scale CS bifurcation that turns the prediction back toward the actual V_L measurement within the main exhaust region. Two very important results may be concluded from this local analysis. First, in this particular case, it would seem that an ~ 10 km s^{-1} offset of the large-scale V_L prediction can be traced to the presence of a second, very narrow CS bifurcation at the edge of the main exhaust. Second,
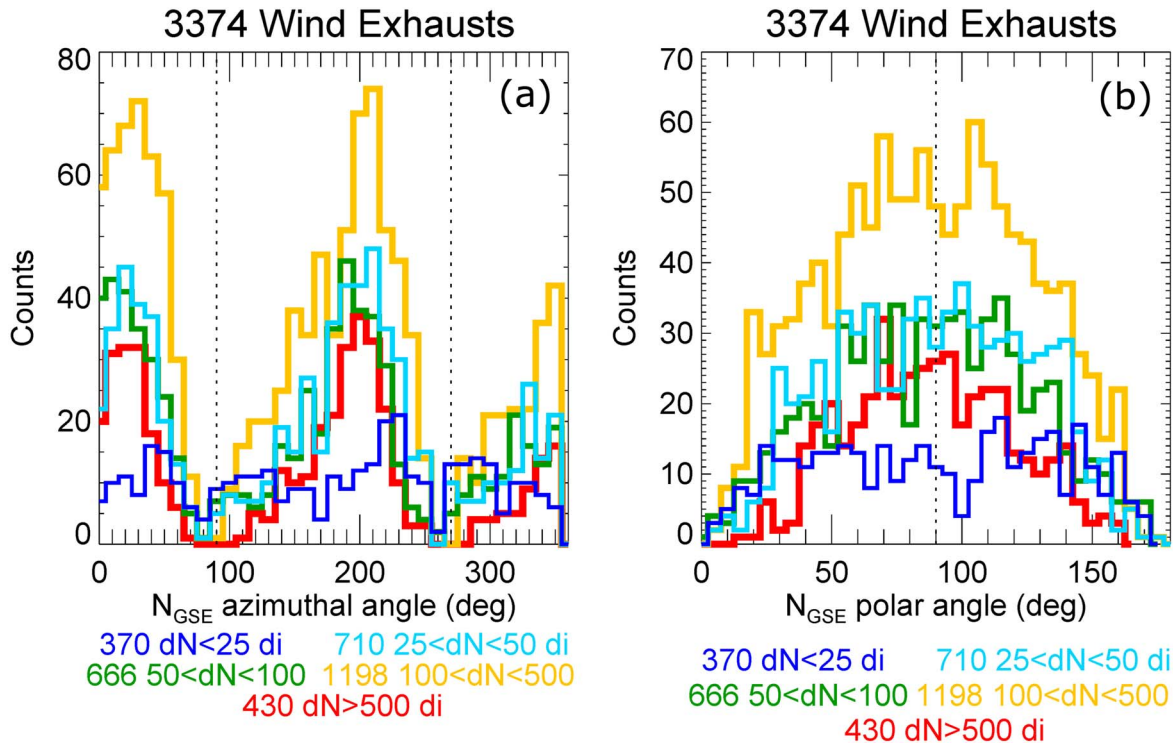
Figure 6. (a) Histograms of 3374 azimuthal angles and (b) polar angles for five subsets of color-coded populations of different CS normal widths as obtained by the Wind spacecraft. The bin sizes are $10°$ wide for the ϕ distribution and $5°$ for the θ distribution, respectively.

despite the availability of only one complete 3DP plasma measurement within this narrow CS, there is a strong indication of a small-scale reconnection exhaust present across this first CS, which is further supported by a bipolar B_{M} variation as shown in Figure 9(c) (left) with the expected sense of a Hall magnetic field. That is, the large-scale CS of 2004 October 8 supported a layered set of several bifurcated CSs, which is present at vastly different spatial scales.

The much wider $d_{\mathrm{cs}} \sim 12{,}233 \, d_i$ exhaust on 2008 July 12 (Figure 8, right) displays a similarly bifurcated super-HCS as the 2004 October 8 event, and it is clearly associated with a secondary bifurcation of the final B_{L} rotation as indicated between the pair of solid green vertical lines at 01:00:00 and 01:07:50 UT as Wind exited the large-scale exhaust boundary. A local $V_{\mathrm{Navg}} \sim 417 \, \mathrm{km \, s}^{-1}$ (see Figure 8(f), right) across this second $\Delta t_{\mathrm{cs}} = 470 \, \mathrm{s}$ or 7.8 minute duration, two-step B_{L} rotation with a $\theta \sim 76°$ magnetic field shear angle corresponds to a $d_{\mathrm{cs}} = 2403 \, d_i$ CS for an average $d_i \sim 82 \, \mathrm{km}$. This two-step CS supports a positive reconnection exhaust (see, e.g., the second V_{WL1} Walén prediction in red and V_{WL2} in blue in Figure 8(d) (right) immediately adjacent to the much larger-scale and negative exhaust. The final, two-step CS is associated with a local $L_{\mathrm{GSE}} = [-0.19957, -0.17395, 0.96432]$, which is deflected by $\sim 31°$ from the primary exhaust L_{GSE} direction, and a local $N_{\mathrm{GSE}} = [-0.85454, -0.45068, -0.25815]$ normal vector, which is only $2.4°$ off the main super-HCS normal direction. Figure 9 (right) displays a detailed view of the initial exhaust-associated CS in its local LMN system (see Table 1) as Wind entered the wide super-HCS region on 12 July 2008. This survey-related, $d_{\mathrm{cs}} = 210 \, d_i$ wide CS from 00:29:10–00:29:54 UT ($\Delta t_{\mathrm{cs}} = 44 \, \mathrm{s}$ between the vertical dashed lines), which is associated with a $\theta \sim 67°$ field rotation, demonstrates a good agreement between the measured $[\Delta V_{\mathrm{L1}}, \Delta V_{\mathrm{L2}}] = [-32.7, -77.8] \, \mathrm{km \, s}^{-1}$ speeds in a local $L_{\mathrm{GSE}} = [-0.47967, 0.87680,$

$-0.03368]$ with the Walén predictions of Figure 9(d) (right). The local $N_{\mathrm{GSE}} = [-0.82146, -0.46223, -0.33399]$ of this initial, short-duration CS is, again, deflected by a small $3.2°$ rotation relative to the N_{GSE} of the main super-HCS. However, the local L_{GSE} direction of this exhaust is deflected by as much as $54°$ from the L_{GSE} of the primary super-HCS. The rather significant L_{GSE} direction offsets of the two edge-associated exhausts explain the apparent V_{M} components of the two jets (see Figure 8(e), right) when displayed in a non-local LMN system of the super-HCS.

Phan et al. (2021) discuss how reconnection exhausts appear to be common across the near-Sun HCS from Parker Solar Probe (PSP) spacecraft observations at heliocentric distances of $29.5–107 \, R_\odot$. They reported normal widths for five well-defined and complete exhaust-associated HCSs near the Sun in a range $d_{\mathrm{cs}} = [240, 890, 1320, 4820, 8220] \, d_i$. Despite this HCS location very close to the Sun, we find that four of the five PSP events fall into the same super-HCS category of 430 Wind events at 1 au (see Figure 8) as the two ACE events summarized in Table 3. The $d_{\mathrm{cs}} = 8220 \, d_i$ PSP event is only $143 \, d_i$ wider than the widest $8077 \, d_i$ event of this Wind survey at 1 au, and it is $\sim 4000 \, d_i$ off from the super-HCS exhaust on 2008 July 12. The relatively narrow $d_{\mathrm{cs}} = 240 \, d_i$ exhaust-related HCS near the Sun is comparable in size with the $d_{\mathrm{cs}} = 210 \, d_i$ exhaust shown in Figure 9 (right), and both events are examples of a population of 1198 exhausts in a category that we refer to as the HCS-like range ($100 \leqslant d_{\mathrm{cs}} < 500 \, d_i$) at 1 au on the basis of a few early HCS studies (Winterhalter et al. 1994; Lepping et al. 1996). It is clear from our extensive survey of 3374 exhausts of many different normal widths (see Figure 6) that reconnection exhausts are not as rare across wide, HCS-like CSs as initially reported at 1 au (e.g., Smith 2001; Gosling et al. 2005b; Phan et al. 2021).
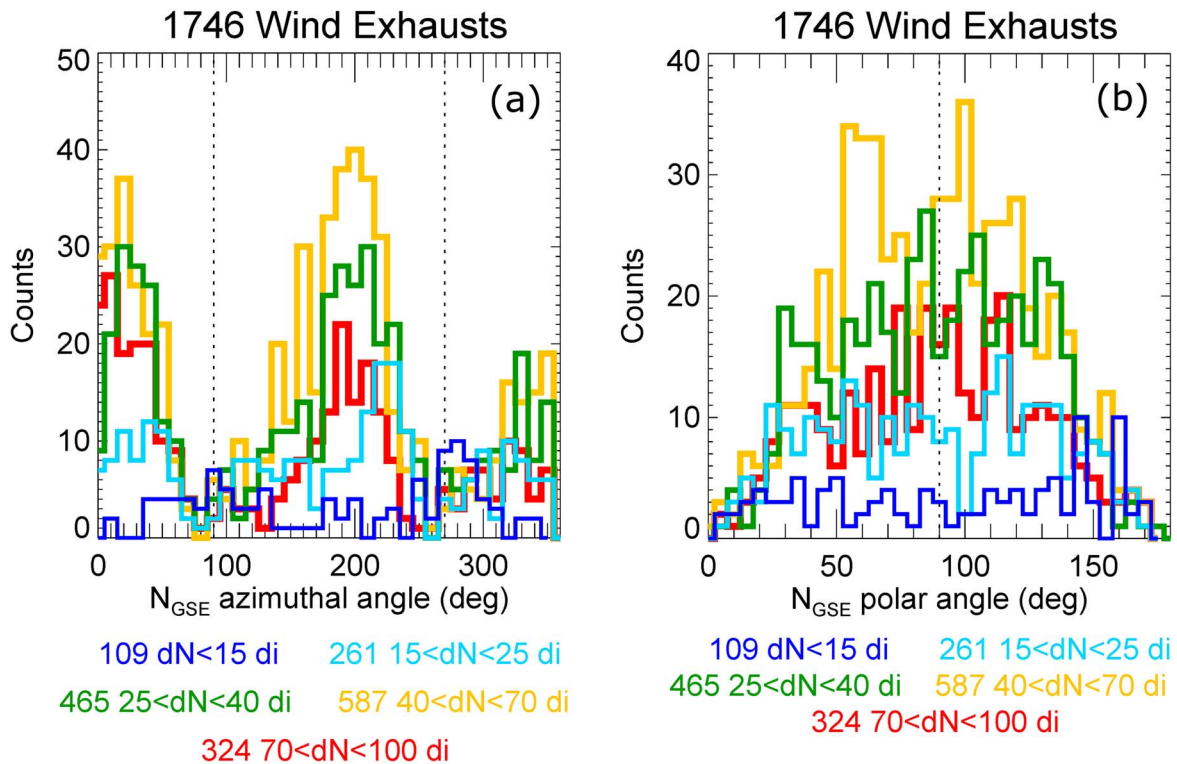
Figure 7. (a) Histograms of 1746 azimuthal angles and (b) polar angles for CS normal widths $d_{cs} < 100\ d_i$ for five color-coded populations of different CS normal widths as obtained by the Wind spacecraft. The bin sizes are $10°$ wide for the ϕ distribution and $5°$ for the θ distribution, respectively. There are 109 exhausts at $d_{cs} < 15\ d_i$ (blue), 261 exhausts at $15 \leqslant d_{cs} < 25\ d_i$ (light blue), 465 exhausts at $25 \leqslant d_{cs} < 40\ d_i$ (green), 587 exhausts at $40 \leqslant d_{cs} < 70\ d_i$ (yellow), and 324 exhausts at $70 \leqslant d_{cs} < 100\ d_i$ (red).

The normal widths of all these HCS-like reconnection exhausts, whether associated with the HCS on the basis of a typical ortho-Parker direction at 1 au (see Figure 6) or confirmed as such from pitch-angle observations of suprathermal strahl electrons at 1 au and near the Sun, are considerably wider than the kinetic scales that we assume to be required for a spontaneous, tearing-unstable, and explosive onset of magnetic reconnection (e.g., Birn et al. 2001). The proposed prevalence of reconnection exhausts across a near-Sun HCS (Phan et al. 2021), and potentially across wide CSs associated with an ortho-Parker direction in the solar wind at 1 au, imply that magnetic reconnection may be triggered by external disturbances near the HCS to support reconnection onset. The presumed turbulent regime adjacent to near-Sun HCSs may be one such trigger mechanism that could potentially allow for a faster rate of reconnection $R > 0.1$ (Lazarian & Vishniac 1999; Lazarian et al. 2020).

4.3 Large-scale Implications of a Two-step Bifurcation of Exhaust-associated CSs

The observation of reconnection exhausts across several wide near-Sun HCS has an important consequence for the observed d_{cs} distribution of reconnection exhausts at 1 au and the realization that CSs with a wide range of normal widths from 15–25 d_i to well beyond 500 d_i are organized by a Parker-spiral magnetic field direction. The implication of reconnection across the near-Sun HCS centers on a common, although not universal, bifurcation of the B_L profile across a CS in this Wind spacecraft distribution of exhausts at 1 au. That is, there are two mostly parallel CSs directed along the M_{GSE} direction at the edges of many reconnection exhausts, rather than one continuous B_L rotation of a broad Harris-type J_M current layer across the entire exhaust. The

two CSs are reflected as the two separate and step-like rotations of the B_L component. The two parallel J_M layers are often separated by a more gradual B_L rotation that often appears as a plateau as, e.g., nicely illustrated by La Belle-Hamer et al. (1995). This bifurcation is clearly present for two kinetic-scale exhausts with normal widths $d_{cs} = 14.5\ d_i$ on 2004 July 9 (Figure 1, left) and $d_{cs} = 22.4\ d_i$ at the edge of a wider exhaust on 2004 October 8 (Figure 9, left). B_L bifurcations are also clear for a sub-HCS scale $d_{cs} \sim 53\ d_i$ asymmetric exhaust on 2010 May 31 (Figure 4, right), two HCS-like exhausts with normal widths $d_{cs} \sim 150\ d_i$ on 2004 Aug 10 (Figure 1, right) and $d_{cs} = 210\ d_i$ on 2008 July 12 (Figure 9, right), and finally the B_L bifurcation of two spectacular super-HCS exhausts on 2004 October 8 ($d_{cs} = 784\ d_i$, Figure 8, left) and 2008 July 12 ($d_{cs} \sim 12233\ d_i$, Figure 8, right). The same B_L bifurcation is present across several of the wide near-Sun HCSs that Phan et al. (2021) report. A CS bifurcation is typically considered as a consequence of the Alfvénic propagation of the magnetic field disturbances along the exhaust separatrix region away from the X-line diffusion region (Gosling & Szabo 2008).

4.3.1. On the Large-scale Evolution of the HCS

We propose that the surprising alignment of narrow exhaust-associated CSs at 1 au with the ortho-Parker azimuthal direction of the large-scale HCS in the ecliptic plane is a consequence of reconnection-mediated CS bifurcation and turbulence within the HCS exhaust. That is, the turbulent fields of the exhaust region may trigger an onset of reconnection (Lazarian & Vishniac 1999) of the two adjacent bifurcated CSs. The proposed HCS-avalanche scenario suggests that the underlying large-scale parent HCS closer to the Sun evolves with heliocentric distance to fracture into many, more or less aligned, secondary CSs due to reconnection.

Table 3
Start (t_1) and Stop (t_2) Date/Times of Two Reconnection Exhausts Associated with the HCS at 1 au as Encountered by the ACE Spacecraft

t_1 (UT)	t_2 (UT)	Δt_{cs} (minutes)	N_{GSE}	L_{GSE}	$|V_N|$ (km s^{-1})	d_{cs} (d_i)	ϕ, θ (°)
19980917/03:17:32	19980917/03:19:48	2.3	[0.98447, 0.17073, −0.04084]	[−0.17400, 0.97985, −0.09812]	303	519	10, 92
19981225/05:34:46	19981225/05:38:32	3.8	[0.75805, 0.59448, −0.26823]	[0.58574, −0.43970, 0.68086]	268	1046	38, 106

Note. The HCS durations Δt_{cs} are listed including N_{GSE} and L_{GSE} and the average normal speed of each HCS to obtain a normal width d_{cs}. The ϕ and θ spherical angles corresponding to N_{GSE} are also listed.
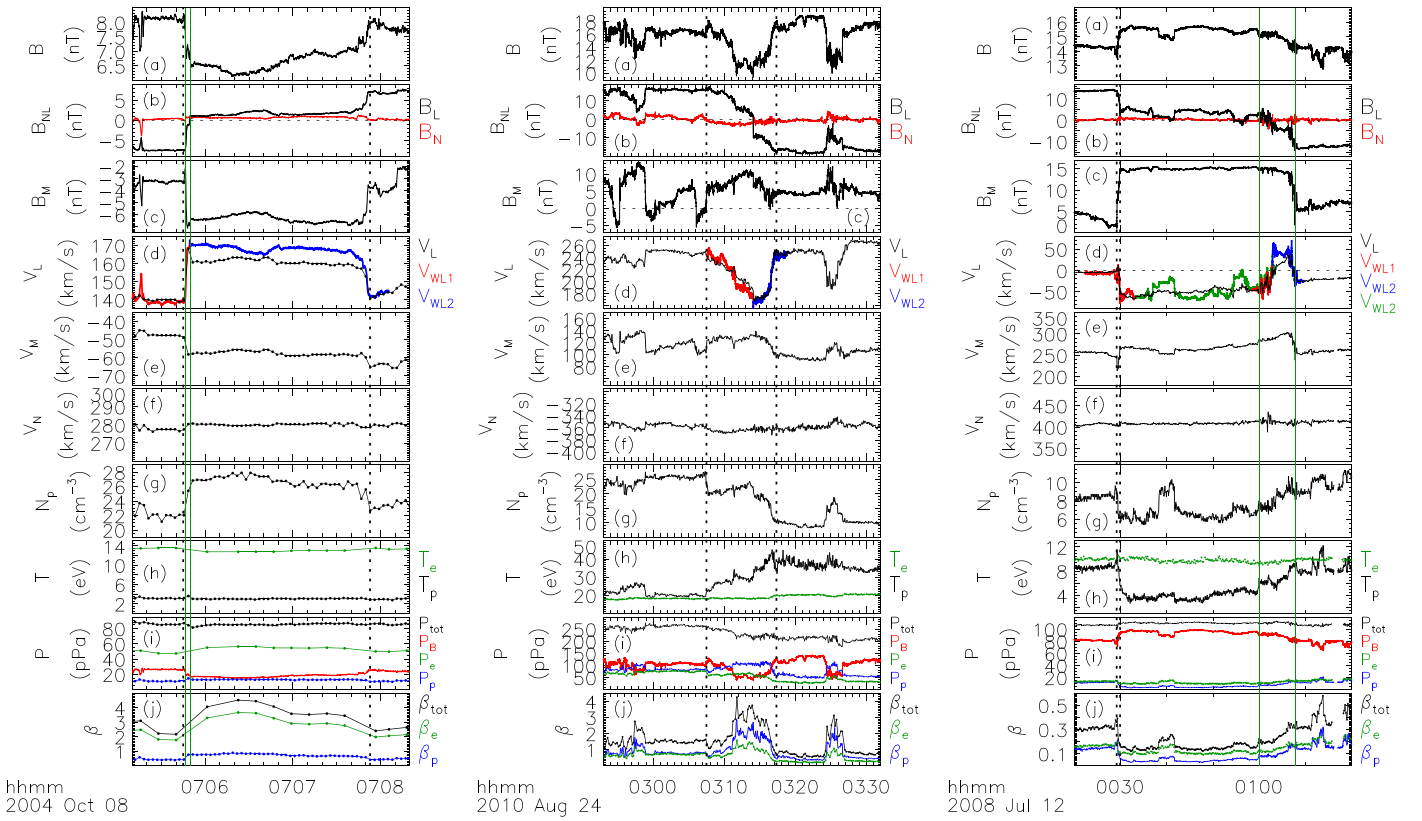
Figure 8. Three examples of Wind reconnection exhausts associated with significant d_{cs} normal widths in the solar wind are shown in their local LMN systems at 07:05:10–07:08:20 UT on 2004 October 8 (left), 02:53:00–03:32:00 UT on 2010 August 24 (middle), and 00:20:00–01:20:00 UT on 2008 July 12 (right). The format is identical to that of Figure 1. A pair of dashed vertical lines mark the B_L rotation of each CS as obtained from an automatic survey. The two green solid vertical lines (left) at 07:05:46.1 UT and 07:05:49.8 UT on 2004 October 8 mark an additional bifurcated CS as Wind entered into a large-scale exhaust region. The pair of green solid vertical lines (right) at 01:00:00 UT and 01:07:50 UT on 2008 July 12 mark an additional bifurcated CS as Wind exited a large-scale exhaust region.

The general CS alignment is further supported by the small $<10°$ deflection between the local N_{GSE} normals of the bifurcated CSs relative to the large-scale parent CS. Each new set of two bifurcated CSs that typically display a lower magnetic field shear angle will have some probability to reconnect driven by the turbulent fields of the adjacent exhaust. This cascade process results in two still smaller-scale exhausts and a set of four CSs, and so on, to explain the HCS alignment of the azimuthal angle distributions down to $15 \leqslant d_{cs} < 25$ d_i that we find in a Wind survey of 3374 reconnection exhausts. Figure 10 summarizes the proposed cascade in a simplified schematic, whereby one HCS reconnects at time t_1 to form two bifurcated CSs adjacent to one wide and primary exhaust at time t_2, with each of the two CSs (J_{M1} and J_{M2}) able to support a bifurcation through secondary magnetic reconnection toward both smaller spatial scales and lower magnetic field shear angles of four exhaust-associated CSs J_1–J_4 at a later time t_4.

The proposed cascade evolution from large to small scales also seems to address the linear increase of the number of exhaust-associated CSs at 1 au from a few high-shear cases at $\theta > 147.5°$ toward a peak at $\theta = 62.5°$ (see Figure 2(h)). Indeed, the apparent drop-off of events for shear angles below $\theta < 40°$ shown in Figure 2(h) could very well originate from an inability to resolve exhausts across kinetic-scale CSs that typically support a very low-shear magnetic field rotation angle (Vasquez et al. 2007; Vasko et al. 2022). The proposed *inside-out* evolution scenario from a set of relatively fewer, but wide exhaust-associated HCSs close to the Sun to a set of many relatively narrow HCS-aligned exhausts at 1 au represents a

different interpretation of the exhaust d_{cs} distribution at 1 au as compared with a notion of ever-expanding jets originating from many kinetic-scale turbulent CSs into a super-HCS $d_{cs} \geqslant 500$ d_i exhaust population in the 1 au solar wind. Shepherd et al. (2017) also caution against an ever-expanding jet evolution, since an out-of-plane guide field component of the magnetic field, which does not participate in the merging process, will force the exhaust to remain collimated in a normal direction beyond a critical distance from the X line. The proposed conceptual framework suggests that the set of much fewer and wider exhaust-associated HCS-like CSs at 1 au could rather represent a population of a few HCSs that failed to reconnect as frequently between the Sun and 1 au as some other HCSs.

Figure 11 displays two additional examples in support of the proposed HCS-avalanche scenario. First, on 2013 May 19 the Wind spacecraft encountered a large-scale CS between 15:53:19.3 and 15:57:42.0 UT associated with a $\theta \sim 130°$ shear angle. Figure 11 (left) marks the two times of this $\Delta t_{cs} \sim 263$ s or 4.4 minute duration CS between the first green vertical line and the second dashed vertical line, which translates to a $d_{cs} \sim 845$ d_i normal width for an average background $V_{Navg} \sim 335$ km s^{-1} and $d_i \sim 104$ km. However, this large-scale CS does not support a single reconnection exhaust at this time in contrast with the earlier events on 2004 October 8 and 2008 July 12. The exhaust survey rather captured a bifurcated CS toward the second edge of this entire CS with a normal $N_{GSE} = [0.87468, 0.21288, 0.43544]$ that we associate with a $d_{cs} \sim 220$ d_i wide exhaust along $L_{GSE} = [0.03437, 0.86889, -0.49381]$ with jet speeds $[\Delta V_{L1}, \Delta V_{L2}] = [19.7, 18.0]$ km s^{-1}, and a $\theta = 63°$ shear angle between the two
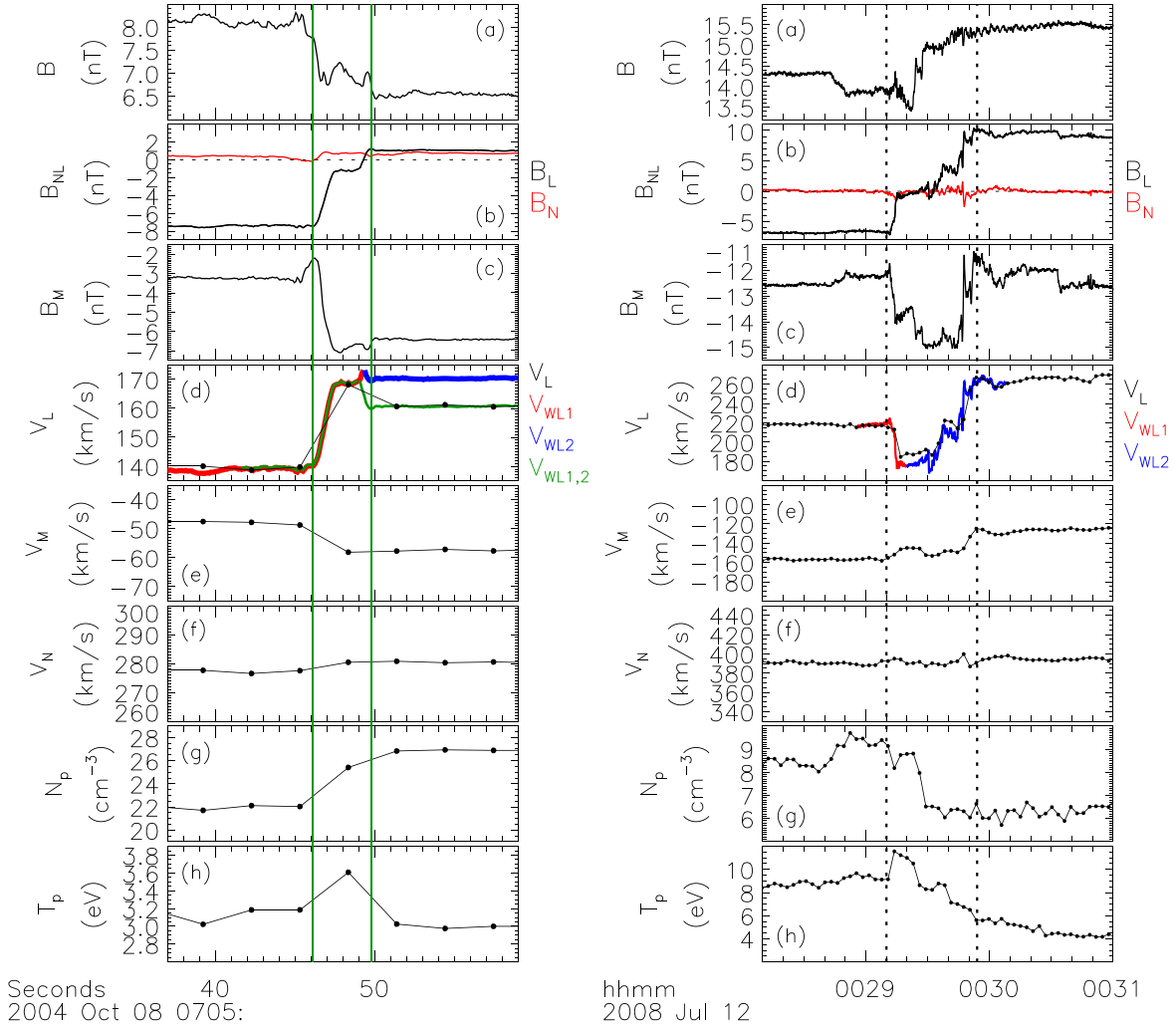
Figure 9. Left: Wind observations are shown at 07:05:37–07:05:59 UT on 2004 October 8 for the same LMN coordinate system that we used for the adjacent larger-scale event of the left-side panels of Figure 8. The panels from the top show (a) | **B**|, (b) B_L (black) and B_N (red), (c) B_M, (d) measured ion velocity V_L (black dots) and predicted ion velocity V_{WL} from the Walén relation in red (V_{WL1} leading edge) and in blue (V_{WL2} trailing edge) associated with the large-scale exhaust and in green color across the entire local CS, (e) V_M, (f) V_N, (g) proton density N_p, (h) proton average temperature T_p. Right: Wind observations at 00:28:10–00:31:00 UT on 2008 July 12 in a local LMN coordinate system (see Table 1). Same panel information as on the left with a local Walén prediction shown in red (V_{WL1} leading edge) and in blue (V_{WL2} trailing edge).

vertical dashed lines at 15:56:36.0 and 15:57:42.0 UT for a local $V_{Navg} \sim 335$ km s^{-1} and $d_i \sim 101$ km. Importantly, the large-scale CS was further fractured into a second pair of CSs across the initial edge of the complete B_L rotation with a local $N_{GSE} =$ [0.81348, 0.40856, 0.41391], $L_{GSE} =$ [−0.45470, 0.00304, 0.89064], and a smaller $\theta \sim 47°$ shear angle between the two green vertical lines at 15:53:19.3 and 15:54:18.0 UT that supported a separate and $d_{cs} \sim 189\ d_i$ wide reconnection exhaust in general agreement with a Walén prediction for a local $V_{Navg} \sim 333$ km s^{-1} and $d_i \sim 103$ km. In other words, this single $\theta \sim 130°$ and $d_{cs} \sim 845\ d_i$ wide CS that Wind encountered on 2003 May 19 was bifurcated, and each of the two lower-shear CSs were in turn bifurcated to support a total of four CSs and two separate reconnection exhausts in a similar positive L_{GSE} direction.

A second intriguing CS provides further support of the proposed HCS-avalanche scenario. This large-scale CS was encountered between 13:05:36.4 and 13:11:42.0 UT on 2012 September 24 and associated with a $\theta \sim 83°$ shear angle. Figure 11 (middle) marks the two times of this $\Delta t_{cs} \sim 366$ s

duration CS between the first green vertical line and the second dashed vertical line, which translates to a $d_{cs} \sim 1108\ d_i$ normal width for an average background $V_{Navg} \sim 279$ km s^{-1} and $d_i \sim 92$ km. However, as with the first event discussed of this nature, the large-scale CS does not support a single reconnection exhaust. The exhaust survey again captured a bifurcated CS toward the second edge of the complete B_L rotation of this CS with a primary normal direction $N_{GSE} =$ [0.80365, 0.39912, 0.44141] that we associate with a $d_{cs} \sim 221\ d_i$ wide exhaust aligned with $L_{GSE} =$ [−0.49770, 0.04414, 0.86622] with jet speeds [ΔV_{L1}, ΔV_{L2}] = [−21.0, −24.2] km s^{-1}, and a $\theta = 61°$ shear angle between the two vertical dashed lines at 13:10:34.0 and 13:11:42.0 UT for a local $V_{Navg} \sim 278$ km s^{-1} and $d_i \sim 86$ km. As with the 2013 May 19 case, the large-scale CS was further fractured across the initial edge of the complete B_L rotation into a second pair of two thinner CSs in a similar direction as the main CS. We associate this additional bifurcated CS with a local $N_{GSE} =$ [0.87012, 0.32393, 0.37143], a local $L_{GSE} =$ [−0.49277, 0.55870, 0.66711] and a smaller $\theta \sim 37°$ shear angle between the two green vertical lines at 13:05:36.4 and 13:07:20.1 UT
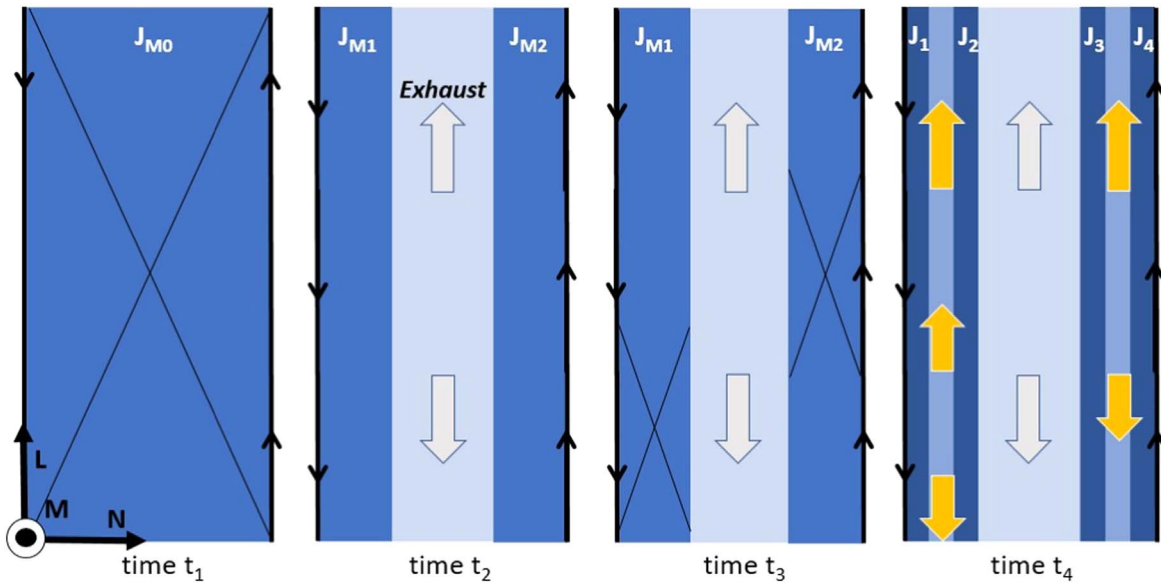
Figure 10. A schematic interpretation of a proposed time evolution ($t_1 < t_2 < t_3 < t_4$) of a cascade process from one large-scale CS to many, typically parallel and small-scale CSs in the solar wind through sequential CS bifurcation associated with magnetic reconnection. It is assumed that all CSs J_{M0}, J_{M1}, J_{M2}, and J_1–J_4 in the regions of dark blue are directed along the out-of-plane $\boldsymbol{M}$ direction for the indicated in-plane directions of the magnetic field ($\boldsymbol{B}$, black arrows). Appearances of reconnection X lines are indicated at times t_1 and t_3 in separate CSs. Two opposite reconnection exhausts are displayed in a spatial region at time t_2, which is bounded by two CSs (J_{M1} and J_{M2}) as a result of a reconnection-mediated CS bifurcation of one original J_{M0}. Subsequent X lines within J_{M1} and J_{M2} at t_3 bifurcates J_{M1} into J_1 and J_2, and J_{M2} bifurcates into J_3 and J_4. Opposite exhausts (yellow) from the subsequent X lines form between the new pair of CSs. All exhaust regions (lighter shades of blue) are assumed to be associated with a plateau of the B_L component of the rotating $\boldsymbol{B}$. A locally more intense CS is expected at the interface of oppositely directed and adjacent exhausts.

that support a separate and wide $d_{cs} \sim 337$ d_i reconnection exhaust in overall agreement with a Walén prediction for a local $V_{Navg} \sim 281$ km s^{-1} and $d_i \sim 86$ km. The $\theta \sim 83°$ and $d_{cs} \sim 1108$ d_i wide primary CS on 2012 September 24 is bifurcated, and each of the two lower-shear CSs were in turn bifurcated to support four CSs in total and what appears as two separate reconnection exhausts. In this case, the two jets were directed in opposite directions relative to the primary $\boldsymbol{L}_{GSE}$ direction.

What makes this 2012 September 24 event exceptionally intriguing, however, is that each of the two initial CSs appear to support a set of two kinetic-scale reconnection exhausts as shown in Figure 11 (right) for the time period 13:05:10–13:07:50 UT. This is especially clear for the $\Delta t_{cs} = 7.3$ s duration CS between 13:07:13.6 and 13:07:20.9 UT that we associate with a local $\theta \sim 29°$ shear angle and a $d_{cs} = 26.7$ d_i normal width in the local LMN system stated above for $V_{Navg} \sim 302$ km s^{-1} and $d_i = 82.5$ km. A local Walén prediction, which is shown here as a red and green curve in Figure 11(d) (right), follows the measured negative V_L jet nearly perfectly as compared with the overall Walén prediction, which is shown as a blue curve. The blue curve clearly overpredicts the measured V_L jet across the complete B_L rotation by about 5–10 km s^{-1} depending on the specific location within this exhaust region. The $\Delta t_{cs} = 3.9$ s duration of the first CS between 13:05:36.4 and 13:05:40.3 UT, with a local $\theta \sim 13°$ shear angle, translates to a kinetic-scale $d_{cs} = 13.2$ d_i normal width for $V_{Navg} \sim 301$ km s^{-1} and $d_i = 89.1$ km. This thin CS, despite being associated with only one complete measurement of the 3DP instrument, does indicate the presence of a positive V_L exhaust from a local Walén prediction (red and green curves). Rather than supporting two exhausts across the full CS, it appears that the initial overpredicted exhaust supports two additional kinetic-scale exhausts with a grand total of four exhausts.

4.3.2. Potential Consequences of a Cascading HCS through Multi-scale Reconnection

The rather common observation that measured exhaust speeds are lower than the predicted exhaust speed in the solar wind (see Figure 2(e)) may potentially be associated with exhaust structure, e.g., magnetic islands that act as an obstacle to the magnetic field and plasma of the L-directed exhaust outflow to force a flow diversion and exhaust deceleration away from the L direction. However, the two large-scale exhaust events of 2004 October 8 (see Figures 8 and 9) and 2012 September 24 (see Figure 11) clearly suggest another plausible explanation in terms of additional small-scale reconnection jets, some of which may not even be resolved by a 3 s cadence plasma measurement. When such small-scale jets are present at the edges of bifurcated and large-scale CSs, they will lead to an overprediction of the large-scale V_L exhaust speed.

The swarm of multiple HCS-like crossings, which are commonly observed at 1 au over a period of 1–2 days around sector boundary encounters (e.g., Crooker et al. 1993, 1996; Winterhalter et al. 1994; Smith 2001), has been explained as a possible extension of multiple parallel CSs from the corona into the heliosphere and associated with multiple helmet streamers (Crooker et al. 1993). The proposed HCS avalanche through turbulence-driven reconnection from within the HCS layer offers an alternative mechanism to explain a swarm of HCS-like crossings around sector boundaries, whereby one HCS is fractured by reconnection into many HCS-like and mostly parallel CSs, with each smaller-scale CS typically associated with a smaller magnetic field shear angle. A major difference between the two mechanisms is that multiple helmet streamers appear to result in a series of parallel CSs of alternating CS direction (Crooker et al. 1993), while an HCS cascade through reconnection is expected to result in a series of parallel CSs in the same general direction.
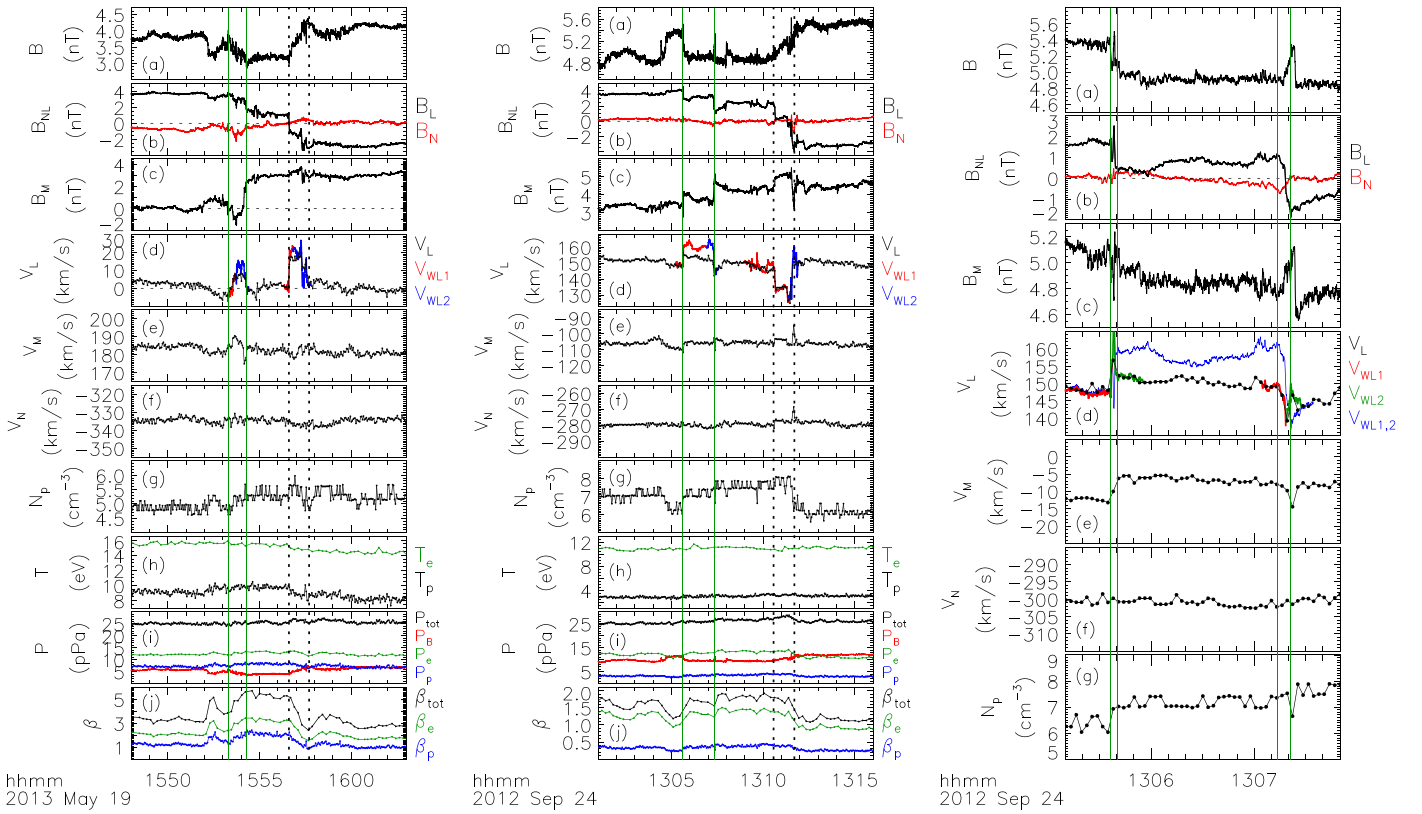
Figure 11. Two examples of Wind reconnection exhausts associated with multiple bifurcated CSs across two large-scale CSs in the solar wind are shown in their local LMN systems at 15:48:00–16:03:00 UT on 2013 May 19 (left) and 13:01:00–13:16:00 UT on 2012 September 24 (middle) for the same panel format as in Figure 1. A pair of vertical dashed lines mark the times (see Table 1) of the exhaust-associated CSs of the survey. A pair of vertical green solid lines mark an additional B_L bifurcation and exhaust at 15:53:19.3–15:54:18.0 on 2013 May 19 (left) and 13:05:36.4–13:07:20.9 UT on 2012 September 24 (middle). The right side panels display a zoomed-in version of the Wind observations at 13:05:10–13:07:50 UT on 2012 September 24, in a local and different LMN system (see the text for vector information) from that used in the middle panels. Here, the two sets of still thinner CSs are marked between a pair of green solid lines at 13:05:36.4–13:05:40.3 and 13:07:13.6–13:07:20.9 UT. See the text for a detailed description of the various Walén predictions (V_{WL}) of the measured V_L exhausts in the (d) panels.

The observed distributions of CS normal orientations (see Figures 5–7) of different CS normal widths suggest that there is a transition region of exhaust-associated CS widths in an approximate range from ∼15 to ∼25 d_i where two populations of CSs coexist in the 1 au solar wind. This range of normal widths appears to represent an upper limit of exhausts associated with a truly turbulent solar wind of isotropic angle distributions of a CS normal direction that likely occurs in between sector boundary traversals. The same transition region also appears to represent a lower limit of the turbulent cascade of the HCS-aligned exhausts at 1 au.

The isotropic distribution of CS exhaust events in the proton kinetic range ($d_{cs} < 25$ d_i) corresponds to a physical scale size of about <2500 km. This value lies within a range of previously published Taylor-scale estimates from two-point turbulent magnetic field measurements, which is about 1400 km (Weygand et al. 2011). The Taylor scale is important here, as it is also the scale at which the damping of turbulent eddies within a turbulent cascade begins to become a dominant force. A tantalizing question, beyond the scope of the present work, is whether the isotropic angular distribution of the CS exhaust normal directions of a proton kinetic range ($d_{cs} < 25$ d_i) is potentially related to the isotropic distribution of the Taylor scale with respect to the mean magnetic field direction.

In order to further characterize the two exhaust populations of the equatorial plane solar wind CSs at 1 au, we explored the

possible impact of magnetic rotation angle θ across the CSs on the distribution of normal widths. Figure 12 displays four nearly equal subsets of the full distribution. The figure only shows histograms below a truncated 250 d_i value due to the extended tails. There were 666 exhausts with a large shear angle $\theta > 115°$ (blue), 928 exhausts with a moderate shear angle $75° < \theta \leqslant 115°$ (light blue), 974 exhausts in a low-shear regime $45° < \theta \leqslant 75°$ (yellow), and 806 exhausts coincided with a very low-shear angle in the range $\theta \leqslant 45°$ (red). The median is $d_{cs} = 45$ d_i for CSs of the very lowest shear angle range. The medians then doubled, first from $d_{cs} = 60$ d_i for low-shear angles ($45° < \theta \leqslant 75°$) to $d_{cs} = 120$ d_i for CSs with moderate shear angles ($75° < \theta \leqslant 115°$), and then nearly doubled again to a median $d_{cs} = 205$ d_i width for CSs of the highest shear ($\theta > 115°$). This trend toward wide and high-shear CSs is in general agreement with the expectation of most of the largest scale HCSs (Lepping et al. 1996). However, it is also clear from Figures 2(h) and 12 that a solar magnetic field may rotate by a relatively smaller angle across HCS-aligned exhaust-associated CSs at 1 au. The smaller field rotation angles $\theta < 180°$ correspond to finite guide-magnetic fields, such that the HCS-like exhausts do not require the solar magnetic field to be oppositely directed on either side of the CS to reconnect. It is very likely that the proposed HCS-avalanche process through reconnection naturally results in this trend toward successively thinner CSs with smaller shear angles. It is also known that narrow, kinetic-scale CSs more typically correspond to very low-shear
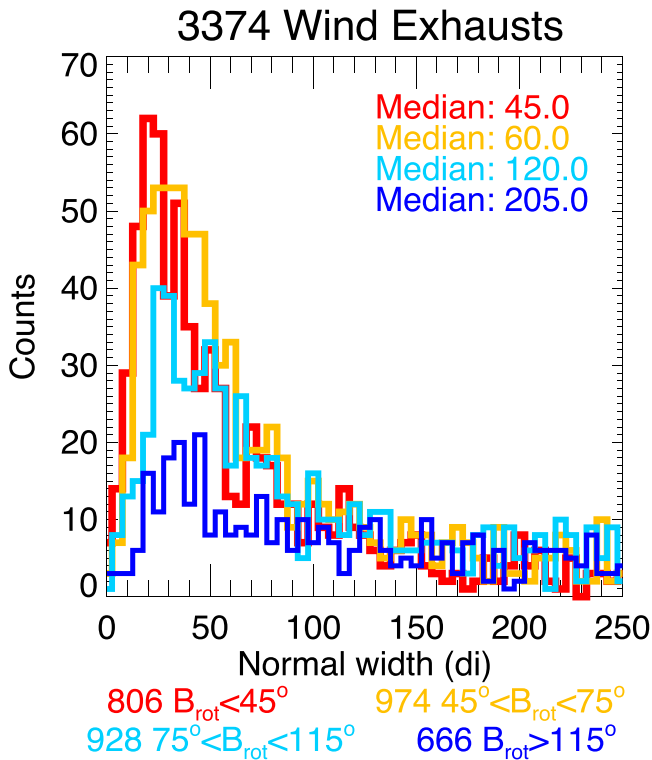
3374 Wind Exhausts

Median: 45.0
Median: 60.0
Median: 120.0
Median: 205.0

806 $B_{rot}<45°$ 974 $45°<B_{rot}<75°$
928 $75°<B_{rot}<115°$ 666 $B_{rot}>115°$

Figure 12. Four histograms of normal widths are displayed for nearly equal subsets of the field rotation angle θ (degrees) of the full distribution of 3374 exhaust-associated CSs. The histograms are truncated at a 250 d_i value due to the extended tails of the distributions. There are 666 exhausts at $\theta > 115°$ (blue), 928 exhausts at $75° < \theta \leqslant 115°$ (light blue), 974 exhausts at $45° < \theta \leqslant 75°$ (yellow), and 806 exhausts at $\theta \leqslant 45°$ (red). The medians of the four distributions with the same 5 d_i bin sizes are stated in the figure.

CSs (Vasquez et al. 2007; Vasko et al. 2022). That is, pure solar wind turbulence likely supports many of the observed very thin exhaust-associated CSs, while the fracturing of HCS-aligned CSs into many different widths as indicated in Figures 6–12 is consistent with turbulence inside the exhausts of active HCSs.

It is not exactly clear why the solar wind would support a transition region of a critical CS dimension at 1 au between the two CS populations, or rather why there is no HCS alignment of CSs below a critical CS width. However, it appears from a Taylor-scale argument that exhausts much wider than $d_{cs} \sim 25$ d_i may be unlikely to evolve from a truly turbulent CS population due to a damping force of turbulent eddies within a turbulent cascade that may start to become important at a Taylor scale of $d_{cs} \sim 14$ d_i or so.

In extending the proposed HCS-avalanche cascade evolution radially outward into the heliosphere, one could expect a fracturing of the HCS to continue with heliocentric distance, perhaps leading to more parallel HCS-like sheets of current that could further bring the critical width of a transition region lower than 25 d_i. That is, the number of HCS-aligned CSs associated with reconnection exhausts could potentially increase from the Sun with an increased number of the very narrow CSs. The expansion of the solar wind volume itself may eventually impact the efficiency of exhaust turbulence to drive magnetic reconnection of bifurcated CSs, while the linearly increasing d_i-scale with heliocentric distance due to the radial profile of the plasma density may impact the transition region in terms of the d_i-scale.

5. Summary and Conclusions

We conclude from the Wind spacecraft observations of 3374 exhausts at the L1 point that the solar wind of the ecliptic plane supports two scale-dependent regimes of reconnection-associated CSs at 1 au. One small-scale CS population exists with normal widths $d_{cs} < 25$ d_i that display an isotropic distribution of CS normal directions in agreement with a source in Alfvénic solar wind turbulence. A second and significantly larger distribution of normal widths $25 < d_{cs} < 8077$ d_i displays a distribution of CS normal directions organized by an ortho-Parker direction in general agreement with a source in a large-scale HCS. It is possible that a turbulent source of exhausts may not support CS widths much larger than $d_{cs} \sim 25$ d_i from a consideration of a Taylor-scale limitation. However, it is unclear why there are so few HCS-aligned exhausts below $d_{cs} \sim 25$ d_i at 1 au. In summary, it appears that there is a transition region around $15 < d_{cs} < 25$ d_i in the 1 au solar wind, where the two CS populations of different source regions may coexist.

We propose that a commonly observed process of CS bifurcation across reconnection exhausts can support a cascade of the HCS from potentially fewer and wider HCSs near the Sun to many often narrower HCS-aligned CSs at 1 au. This is in general agreement with the obtained field shear angle distribution. Several Wind spacecraft examples were presented in support of the proposed HCS-avalanche process, which is summarized in a Figure 10 schematic, whereby one HCS reconnects to form two bifurcated CSs adjacent to one wide and primary exhaust, with each of the two CSs supporting a cascading bifurcation process through secondary magnetic reconnection toward smaller scales and lower magnetic field shear angles of exhaust-associated CSs. Some events of this cascading nature apparently support jets in both L directions immediately adjacent to a large-scale exhaust. Other events simply display an absence of a large-scale exhaust, for unknown reasons, and rather support two spatially removed exhausts toward the edges of the large-scale CS.
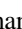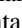
Examples of a localized Walén prediction of the measured V_L component of the solar wind velocity strongly suggest that some cases of overpredicted reconnection exhausts are associated with a presence of bifurcated CSs and localized jets at the exhaust edges. Very small-scale exhaust-associated CS bifurcations can thus impact the predicted V_L flows at much larger scales.

It is possible that turbulence within the HCS exhaust region may be driving this secondary reconnection of the two bifurcated, and nearly parallel CSs, at the exhaust boundary to explain a general alignment of the normal of exhaust-associated CSs with the ortho-Parker spiral direction. The presence of fewer, but wider, exhaust-associated CSs at 1 au may simply reflect a population of HCSs that failed to reconnect as frequently between the Sun and 1 au as some other HCSs. In the sense of a reconnection-driven HCS avalanche, it may be concluded that magnetic reconnection and the downstream exhausts may lead to an intermittent turbulent behavior of the solar wind for spatial scales larger than $d_{cs} \sim 25$ d_i.

The commonly reported swarm of HCS crossings over several days surrounding sector boundaries at 1 au may in certain cases be linked to the proposed reconnection-driven HCS-avalanche process as an alternative to multiple parallel CSs of alternating current direction, which has been proposed to extend out to 1 au from multiple helmet streamers of the solar corona.

ORCID iDs

Stefan Eriksson ● https://orcid.org/0000-0002-5619-1577
Marc Swisdak ● https://orcid.org/0000-0002-5435-3544
James M. Weygand ● https://orcid.org/0000-0001-7996-2277
Alfred Mallet ● https://orcid.org/0000-0001-9202-1340
David L. Newman ● https://orcid.org/0000-0003-0810-1204
Giovanni Lapenta ● https://orcid.org/0000-0002-3123-4024
Lynn B. Wilson III ● https://orcid.org/0000-0002-4313-1970
Drew L. Turner ● https://orcid.org/0000-0002-2425-7818
Bjorn Larsen ● https://orcid.org/0000-0001-6436-8216

References

Alfvén, H. 1977, RvGeo, 15, 271
Angelopoulos, V., Cruce, P., Drozdov, A., et al. 2019, SSRv, 215, 9
Banaszkiewicz, M., Axford, W. I., & McKenzie, J. F. 1998, A&A, 337, 940
Birn, J., Drake, J. F., Shay, M. A., et al. 2001, JGR, 106, 3715
Borrini, G., Gosling, J. T., Bame, S. J., Feldman, W. C., & Wilcox, J. M. 1981, JGR, 86, 4565
Bruno, R., & Carbone, V. 2013, LRSP, 10, 2
Burch, J. L., Moore, T. E., Torbert, R. B., & Giles, B. L. 2016a, SSRv, 199, 5
Burch, J. L., Torbert, R. B., Phan, T. D., et al. 2016b, Sci, 352, 6290
Cassak, P. A., & Otto, A. 2011, PhPl, 18, 074501
Chang, Q., Xu, X., Xu, Q., et al. 2019, ApJ, 884, 102
Chen, C. H. K., Mallet, A., Schekochihin, A. A., et al. 2012, ApJ, 758, 120
Cho, J., & Lazarian, A. 2009, ApJ, 701, 236
Cranmer, S. R. 2009, LRSP, 6, 3
Crooker, N. U., Burton, M. E., Siscoe, G. L., et al. 1996, JGR, 101, 24331
Crooker, N. U., Siscoe, G. L., Shodhan, S., et al. 1993, JGR, 98, 9371
Davis, M. S., Phan, T. D., Gosling, J. T., & Skoug, R. M. 2006, GeoRL, 33, L19102
Dong, C., Wang, L., Huang, Y. M., Comisso, L., & Bhattacharjee, A. 2018, PhRvL, 121, 165101
Drake, J. F., Antonsen, T. M., Hassam, A. B., & Gladd, N. T. 1983, PhFl, 26, 2509
Enžl, J., Přech, L., Šafránková, J., & Němeček, Z. 2014, ApJ, 796, 21
Eriksson, S., Gosling, J. T., Phan, T. D., et al. 2009, JGR, 114, A07103
Eriksson, S., Lapenta, G., Newman, D. L., et al. 2015, ApJ, 805, 43
Eriksson, S., Newman, D. L., Lapenta, G., & Angelopoulos, V. 2014, PPCF, 56, 064008
Eriksson, S., Wilder, F. D., Ergun, R. E., et al. 2016, PhRvL, 117, 015001
Gloeckler, G., Cain, J., Ipavich, F. M., et al. 1998, SSRv, 86, 497
Gosling, J. T. 2007, ApJ, 671, L73
Gosling, J. T., Borrini, G., Asbridge, J. R., et al. 1981, JGR, 86, 5438
Gosling, J. T., Eriksson, S., Phan, T. D., et al. 2007a, GeoRL, 34, L06102
Gosling, J. T., Eriksson, S., & Schwenn, R. 2006b, JGRA, 111, A10102
Gosling, J. T., Eriksson, S., Skoug, R. M., McComas, D. J., & Forsyth, R. J. 2006a, ApJ, 644, 613
Gosling, J. T., McComas, D. J., Skoug, R. M., & Smith, C. W. 2006c, GeoRL, 33, L17102
Gosling, J. T., & Phan, T. D. 2013, ApJL, 763, L39
Gosling, J. T., Phan, T. D., Lin, R. P., & Szabo, A. 2007b, GeoRL, 34, L15110
Gosling, J. T., Skoug, R. M., McComas, D. J., & Smith, C. W. 2005a, JGRA, 110, A01107
Gosling, J. T., Skoug, R. M., McComas, D. J., & Smith, C. W. 2005b, GeoRL, 32, L05105
Gosling, J. T., & Szabo, A. 2008, JGR, 113, A10103
Jokipii, J. R., & Thomas, B. T. 1981, ApJ, 243, 1115
Klein, K. G., & Vech, D. 2019, RNAAS, 3, 107
Knetter, T., Neubauer, F. M., Horbury, T., & Balogh, A. 2004, JGR, 109, A06102
La Belle-Hamer, A. L., Otto, A., & Lee, L. C. 1995, JGR, 100, 11,875
Lakhina, G. S., & Schindler, K. 1983, Ap&SS, 89, 293
Lapenta, G. 2008, PhRvL, 100, 235001
Lapenta, G., & Lazarian, A. 2012, NPGeo, 19, 251
Lazarian, A., & Vishniac, E. T. 1999, ApJ, 517, 700
Lazarian, A. G. L., Eyink, A., Jafari, G., et al. 2020, PhPl, 27, 012305
Lepping, R. P., Acũna, M. H., Burlaga, L. F., et al. 1995, SSRv, 71, 207
Lepping, R. P., Szabo, A., Peredo, M., & Hoeksema, J. T. 1996, GeoRL, 23, 1199
Lin, R. P., Anderson, K. A., Ashford, S., et al. 1995, SSRv, 71, 125
Lionello, R., Velli, M., Downs, C., Linker, J. A., & Mikić, Z. 2014, ApJ, 796, 111
Loureiro, N. F., & Boldyrev, S. 2017, ApJ, 850, 182
Luhmann, J. G., Zhang, T.-L., Petrinec, S. M., et al. 1993, JGR, 98, 5559
Mallet, A., Schekochihin, A. A., Chandran, B. D. G., et al. 2016, MNRAS, 459, 2130
Mallet, A., Schekochihin, A. A., & Chandran, B. D. G. 2017, MNRAS, 468, 4862
Marsch, E. 1999, SSRv, 87, 1
Matthaeus, W. H., & Goldstein, M. L. 1982, JGR, 87, 6011
Matthaeus, W. H., & Lamkin, S. L. 1986, PhFl, 29, 2513
McComas, D. J., Bame, S. J., Barker, P., et al. 1998, SSRv, 86, 563
Mistry, R., Eastwood, J. P., Haggerty, C. C., et al. 2016, PhRvL, 117, 185102
Mistry, R., Eastwood, J. P., Phan, T. D., & Hietala, H. 2017, JGRA, 122, 5895
Ogilvie, K. W., Chornay, D. J., Fritzenreiter, R. J., et al. 1995, SSRv, 71, 55
Osman, K. T., Matthaeus, W. H., Gosling, J. T., et al. 2014, PhRvL, 112, 215002
Parker, E. N. 1958, ApJ, 128, 664
Paschmann, G., Papamastorakis, I., Baumjohann, W., et al. 1986, JGR, 91, 11099
Phan, T. D., Bale, S. D., Eastwood, J. P., et al. 2020, ApJS, 246, 34
Phan, T. D., Gosling, J. T., Davis, M. S., et al. 2006, Natur, 439, 175
Phan, T. D., Gosling, J. T., & Davis, M. S. 2009, GeoRL, 36, L09108
Phan, T. D., Gosling, J. T., Paschmann, G., et al. 2010, ApJL, 719, L199
Phan, T. D., Lavraud, B., Halekas, J. S., et al. 2021, A&A, 650, A13
Phillips, J. L., Bame, S. J., Feldman, W. C., et al. 1995, Sci, 268, 1030
Priest, E., & Forbes, T. 2000, in Magnetic Reconnection: MHD Theory and Applications (New York: Cambridge Univ. Press)
Pulupa, M. P., Salem, C., Phan, T. D., Gosling, J. T., & Bale, S. D. 2014, ApJL, 791, L17
Retinò, A., Sundkvist, D., Vaivads, A., et al. 2007, NatPh, 3, 235
Schulz, M. 1973, Ap&SS, 24, 371
Servidio, S., Matthaeus, W. H., Shay, M. A., et al. 2010, PhPl, 17, 032315
Servidio, S., Matthaeus, W. H., Shay, M. A., Cassak, P. A., & Dmitruk, P. 2009, PhRvL, 102, 115003
Servidio, S., Valentini, F., Califano, F., & Veltri, P. 2012, PhRvL, 108, 045001
Shepherd, L. S., Cassak, P. A., Drake, J. F., et al. 2017, ApJ, 848, 90
Smith, C. W., L'Heureux, J., Ness, N. F., et al. 1998, SSRv, 86, 613
Smith, E. J. 2001, JGR, 106, 15,819
Sonnerup, B. U. Ö., & Cahill, L. J., Jr. 1967, JGR, 72, 171
Sonnerup, B. U. Ö., Paschmann, G., Papamastorakis, I., et al. 1981, JGR, 86, 10,049

Sonnerup, B. U. Ö., & Scheible, M. 1998, in ISSI Sci. Rep. SR-001, Analysis Methods for Multi-Spacecraft Data, ed. G. Paschmann & P. W. Daly (Noordwijk: ESA Publications Division), 185

Swisdak, M., Opher, M., Drake, J. F., & Alouani Bibi, F. 2010, ApJ, 710 1769

Swisdak, M., Rogers, B. N., Drake, J. F., & Shay, M. A. 2003, JGR, 108, A5

Vasko, I. Y., Alimov, K., Phan, T. D., et al. 2021, ApJL, 923, L19

Vasko, I. Y., Alimov, K., Phan, T., et al. 2022, ApJL, 926, L19

Vasquez, B. J., Abramenko, V. I., Haggerty, D. K., & Smith, C. W. 2007, JGR, 112, A11102

Webster, J. M., Burch, J. L., Reiff, P. H., et al. 2018, JGRA, 123, 4858

Weygand, J. M., Matthaeus, W. H., Dasso, S., & Kivelson, M. G. 2011, JGR, 116, A08102

Wilson, L. B., Brosius, A. L., Gopalswamy, N., et al. 2021, RvGeo, 59, e2020RG000714

Wilson, L. B., Stevens, M. L., Kasper, J. C., et al. 2018, ApJS, 236, 41

Winterhalter, D., Smith, E. J., Burton, M. E., Murphy, N., & McComas, D. J. 1994, JGR, 99, 6667

Zhdankin, V., Uzdensky, D. A., Perez, J. C., & Boldyrev, S. 2013, ApJ, 771, 124